March 25, 2026

Peer review for WES-2025-148
Title: ”Wind-field estimation for lidar-assisted control: A comparison of proper orthogonal decomposition and interpolation techniques”

Dear Referees,

We sincerely thank the referees for their time and careful review of the manuscript. Your insightful comments and constructive feedback have improved the clarity and overall quality of the paper.

We have considered each comment and revised the manuscript accordingly. Below, we provide point-by-point responses to all comments.

For your convenience, we have also included a marked-up version of the revised manuscript showing all changes in blue.

Sincerely,

The Authors

Correspondence: Esperanza Soto Sagredo (espa@dtu.dk)

Comments Referee # 1

Comment 1: Simulations are not driven through Coriolis forcing. I wonder how this impacts the development of sheer and veer in the simulated ABL.

Response:
Generally, the sheer is governed by the roughness, while veer stems from a combination of Coriolis and height of the inversion. So without Coriolis there will be no significant veer, see Kelly and van der Laan (2023).

Comment 2: What happens when the atmospheric conditions deviate from these boundary conditions? Is there any way to infer impacts to the inflow estimation quality?

Response:
This question is related to Comment 5, so please refer to our response below.

Comment 3: Does this rescaling apply to the turbulent content of the inflow or is the mapping identical for mean velocity profile and turbulence?

Response:
The scaling using Eq. 1 is applied on the full flow, i.e. including the turbulent content.

Comment 4: In assessing the validity of Taylor's hypothesis in this case, what is the turbulence intensity for the flow? More importantly, what impact will the mean shear gradient and veer have on the resulting 3D turbulent inflow fields? Is a new global basis defined for each inflow scaled as per eq. 1, or is the global basis universal for all inflows with $u_{\text{new}} \in [8.0, 12.0, 15.0, 18.0]$ ms^{-1}

Response:
As previously mentioned, the absence of Coriolis implied that there is no significant veer and the shear gradient governed by the relative roughness. The turbulence is shear generated, and therefore the turbulent structures and magnitude of turbulence intensity will vary with height. The global basis is universal for all inflows (in the selected study). So "global" and "universal" is the same.

Comment 5: An important consideration when using a global basis of POD modes must be, "how representative is this basis for the flow in question?" Certainly we expect that modes defined from the ensemble of cases should be a good representation of the dynamics for each individual case unless there's some reason to question the statistical stationarity of the larger simulation. More generally, can the methods used in this work generalize to using the same global basis for cases where the background atmospheric changes have changed (e.g., for non-neutral conditions)?

Response:
Yes, exactly. The current study hinges on a global basis that is representative. Céspedes Moreno et al. (2025), showed that it is possible to derive global bases that efficiently represent different flow scenarios for wind turbine wakes. It remains an open question how effective a global basis can been for very different atmospheric conditions, e.g. different stability conditions, and we are actively working on addressing this larger question in other studies. As a preliminary inference based on experience, we would expect the efficiency

to depend on the rotor size, i.e. it will be easier to derive an efficient global basis covering a small turbine as the spatial variations are smaller than for a very large turbine, which might encounter inversion, low-level jets or other asymmetric conditions.

Comment 6: The basis of global modes shown in Appendix B show behavior similar to 2D Fourier modes, consistent with a nearly uniform background flow. Is this expected? The text does not indicate the shear exponent or veer across the considered domain. These non-homogeneities would likely result in more complex behavior in the global modes.

Response:
Yes, it is to be expected to POD modes resemble Fourier modes, as pointed out in the seminal work by Lumley (1967), and more recently investigated by Hodzic et al. (2024). The minor deviations from Fourier modes are precisely due to non-homogeneities, where there is a vertical change in the turbulent structures as explained in response to comment 4. This is most evident in modes 6-9 (Appendix B, Fig. B1), where the red (and blue) colors (and hence contours) are stronger near the ground than at the top.

Comment 7: Does the rotational velocity of the rotor also need to be accounted for in the motion correction or does considering only the u component of velocity assume away the problem? I understand that no motion correction was applied in the end, but for completeness, it would be good to include a statement as to why it should be considered or can safely be neglected.

Response: Projecting the line-of-sight (LOS) velocity onto the longitudinal direction does not eliminate motion-induced contamination. If motion correction is desired, it must be applied at the LOS level by subtracting the component of the sensor/platform velocity projected onto the beam direction.

In principle, both tower/nacelle motion and rotor rotation can introduce relative-velocity terms. In the current HAWC2 hub-lidar implementation, the sensor kinematics include tower motion (and therefore, tower relative velocity effects on the lidar measurements), but does not include an additional translational contribution associated with rotor tangential velocity.

In the study we do not apply an explicit tower-motion correction. While a point-wise real-time correction is possible in principle, it would require accurate platform-velocity estimates for each lidar acquisition (e.g., from accelerometers sensors and subsequent integration), which is nontrivial and may introduce additional uncertainty. Instead, consistent with common practice in lidar-assisted control (LAC), motion-related artifacts are typically mitigated via low-pass and/or band-stop filtering prior to using reconstructed inflow fields for control (Schlipf, 2016; Gräfe et al., 2023).

Accordingly, we treat motion-corrupted measurements as part of the overall measurement-uncertainty chain and evaluate reconstruction accuracy in the presence of these effects. Because the reconstructed inflow fields are not used directly for LAC actions or load assessment in this manuscript, our focus remains on inflow reconstruction accuracy while retaining the associated uncertainties.

We have clarified these points in Sect. 2.4 (paragraphs 200–205) and in Sect. 3.2.3, and we also note that off-axis optics may introduce an additional rotational contribution. In practical deployments, tower motion and rotational effects can become non-negligible and should be addressed through motion correction and/or filtering before using reconstructed inflow fields for load assessment or LAC.

Comment 8: Should be M_{lidar}?

Response: If this comment refers to the notation in Sect. 2.7.2, we have corrected it (the second term was not typeset consistently). The revision is shown in blue in paragraph 300.

Comment 9: This method shares some elements with that of Beck H, Kühn M. Temporal Up-Sampling of Planar Long-Range Doppler LiDAR Wind Speed Measurements Using Space-Time Conversion. Remote Sensing. 2019; 11(7):867 (Beck and Kühn, 2019).

Response: We thank the reviewer for pointing out (Beck and Kühn, 2019). We have added this reference in Sect. 1 (paragraph 80).

Comment 10: It's not clear to me why the baseline method should miss the low-frequency content of the velocity spectra regardless of the number of scans considered, when all the other methods make a nearly perfect match. Additional interpretation would be appreciated.

Response: Figures 7 and 8 (Sect. 3.2.1) presents the power spectral density (PSD) computed independently at each grid point within the circular area of interest, A_R, defined by $\sqrt{y_j^2 + (z_j - z_{\text{hub}})^2} \leq 95$ m, centered at hub height, where the locations included in this aggregation are represented by the orange dots shown in Fig. 2. Therefore, the resulting PSDs are averaged as follow:

$$\text{PSD}_{\text{avg}} = \frac{1}{N} \sum_{i=1}^{N} S_{ii}(f) \tag{1}$$

Since each $S_{ii}(f)$ captures the full variance of $u_{ij}(t)$ at that location, including the spatial variability across the rotor plane, this approach provides a better estimation and visualization of the goal of the reconstruction methodologies, which is to characterize the wind speed variations across the full rotor plane at each time step.

Figure 1 shows five 10-min time series at five rotor-plane grid locations in the y–z plane (highlighted in blue in Fig. 2), together with the corresponding PSDs for the reconstruction methods, using $\theta = 22.5°$, $n_{\text{scan}} = 4$ for the selection window, and $K = 50$ POD modes for the POD-based methods. Across all locations, the baseline (blue curve) produces point-wise time series that are systematically smoother than the full LES and the spatial reconstruction methods. This behavior is evident in the point-wise PSDs in Fig. 1 (right panels) and leads to reduced energy in the corresponding point-wise and aggregated spectra, including at low frequencies.

Importantly, this behavior is specific to spatially resolved statistics. When the PSD is evaluated for the rotor-averaged wind speed (RAWS), which is the quantity the baseline is intended to reproduce, the baseline captures the low- and mid-frequency content well (Fig. 3, panel (b)), similarly to the proposed reconstruction methods.

Further clarification of the baseline PSD estimation and behavior has been added to the manuscript in Sect. 3.2 (paragraph 400) and Sect. 3.2.1 (Low frequencies; paragraph 420).

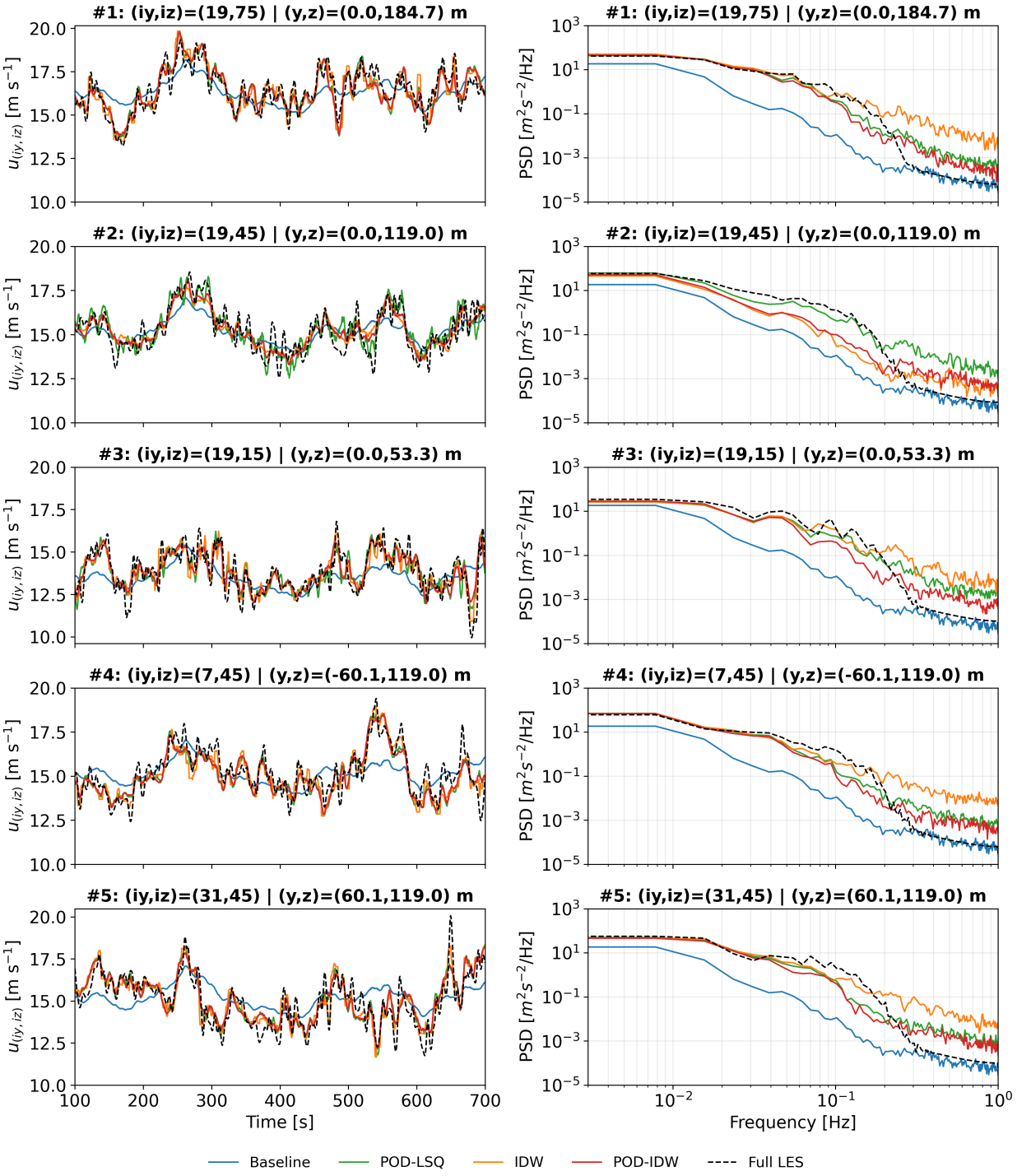

Figure 1: Point-wise comparison at representative grid locations: time series (left) and corresponding spectra (right) for the baseline and spatial reconstruction methods relative to the full LES. The baseline (blue lines) produces smoother point-wise signals and reduced spectral energy, including at low frequencies, consistent with its rotor-equivalent formulation.

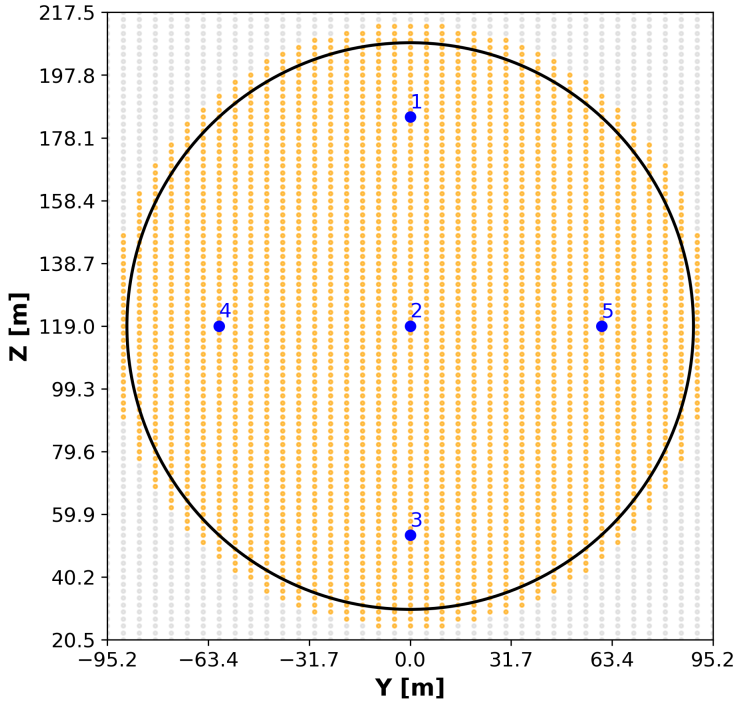

Figure 2: Grid points in the y–z plane used to generate the reconstructed inflow fields. Orange markers indicate the grid points used for the spectral aggregation in Sect. 3.2.1, i.e., points within the circular region A_R defined by $\sqrt{y_j^2 + (z_j - z_{\text{hub}})^2} \leq 95$ m and centered at hub height. Blue markers indicate the five grid locations used for the point-wise time series shown in Fig. 1.

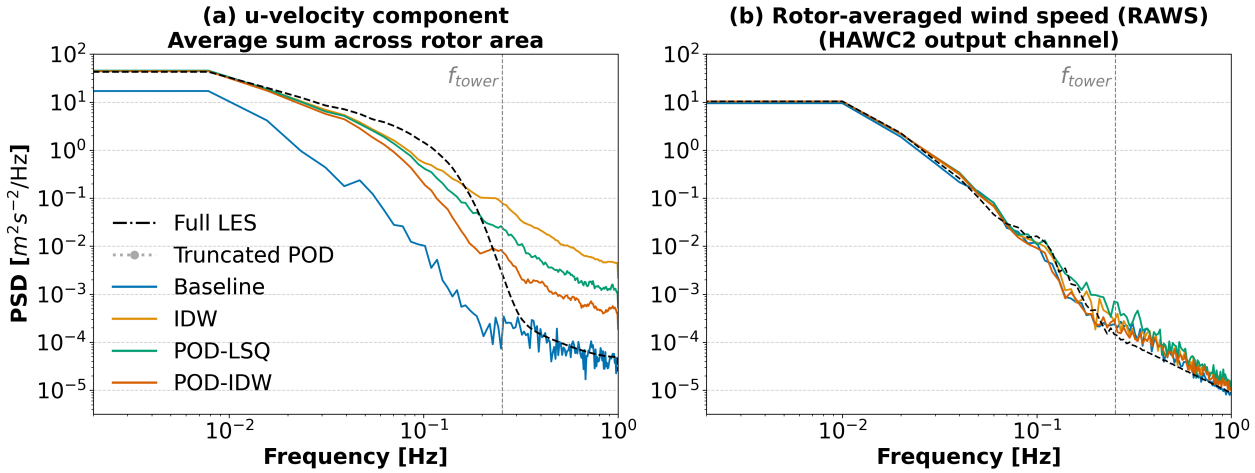

Figure 3: Turbulence spectra from a 10-min simulation for each method using $\theta = 22.5°$, $n_{\text{scan}} = 4$, and $K = 50$ global POD modes for the POD-based methods, with the volume-averaged lidar estimate ($u_{\text{lidar,wgh}}$) as input. (a) PSD of the spatially resolved u-component aggregated over the rotor area A_R. (b) PSD of the rotor-averaged wind speed (RAWS) extracted from the HAWC2 output channel for aeroelastic simulations driven by the reconstructed inflows. PSDs are estimated using Welch's method with a Hamming window (six segments, 50% overlap).

Comment 11: Figure 7. Is there any way to relate the spectra to the MAE for each case? The spectra themselves describe the distribution of energy across a range of frequencies, but it's not clear how the missing energy in the mid-range or the extra energy for high frequencies might influence the MAE.

Response: Two reconstructions may exhibit similar PSDs but different phases, leading to different instantaneous deviations and therefore different mean absolute error (MAE) values. Moreover, for the proposed reconstruction methods, different sources of uncertainty can increase energy in the mid-frequency range (Sect. 3.2), which may yield good agreement with the full LES PSD while producing a noisier time-domain signal and, consequently, a higher MAE.

This effect is evident in Fig. 1 and Table 1, which presents the MAE for the five time series presented in this figure. At location #2 (hub height), POD–LSQ produces a noisier signal because no measurements are available near the rotor center for that case, which makes the least-squares fit more sensitive and increases the local error (MAE$= 0.551$ m s^{-1}). Although the POD–LSQ PSD shows comparatively good agreement with LES reference at low and mid frequencies, this does not imply a more accurate time-domain estimate. In contrast, POD–IDW provides the lowest error at location #2 (MAE $= 0.500$ m s^{-1}), despite underestimating part of the mid-frequency energy.

Table 1: Mean absolute error (MAE) over 10 minute time series presented in Fig. 1, at locations displayed as blue dots in Fig. 2, against the LES reference case.

Location	Baseline	POD-LSQ	IDW	POD-IDW
# 1: $y = 0$ m, $z = 184.7$ m	0.760 ms^{-1}	0.472 ms^{-1}	0.453 ms^{-1}	0.480 ms^{-1}
# 2: $y = 0$ m, $z = 119.0$ m	0.699 ms^{-1}	0.551 ms^{-1}	0.522 ms^{-1}	0.500 ms^{-1}
# 3: $y = 0$ m, $z = 53.3$ m	0.878 ms^{-1}	0.529 ms^{-1}	0.495 ms^{-1}	0.498 ms^{-1}
# 4: $y = -60.1$ m, $z = 119.0$ m	0.811 ms^{-1}	0.568 ms^{-1}	0.514 ms^{-1}	0.559 ms^{-1}
# 5: $y = 60.1$ m, $z = 119.0$ m	1.077 ms^{-1}	0.560 ms^{-1}	0.532 ms^{-1}	0.561 ms^{-1}

Accordingly, Figs. 7–8 are used as diagnostics to interpret how key parameters (e.g., scan count, POD mode truncation, and measurement uncertainties) affect the spectral energy content of each method, rather than serving as predictors of accuracy.

In particular, missing energy over a frequency band indicates that the reconstructed signal is over-smoothed (i.e., fluctuations are attenuated) relative to the LES. In this study, such attenuation can arise from lidar probe-volume effects and from additional spatial filtering introduced by the multi-distance measurement-selection approach: increasing n_{scan} typically increases measurement availability and can improve reconstruction (and reduce methodology uncertainty), but it also expands the scan-selection window and enhances turbulence filtering.

Comment 12: Tower natural frequency. Does the presence of the tower natural frequency in the inflow spectra suggest that the observations should be motion compensated? The peak is only visible in the virtual lidar measurements, not in the true wind speed.

Response: This point is addressed in Comment 7. We note for completeness that the manuscript already states this explicitly at the end of Sect. 3.2.3: "Finally, attention should be given to the effects of tower motion, which introduce spurious energy near the tower's

natural frequency (f_{tower}). These artifacts, particularly prominent in lidar-based reconstructions, require correction techniques or frequency-domain filtering to avoid negative impacts on both control performance and aeroelastic load assessments."

Comment 13: Figure 8. Similar to the comment for Figure 7, it's not clear how to consider the spectra in terms of the MAE. Results below suggest that the POD-IDW method produces lower values of MAE, even though the spectra in Figure 8 show a worse match to the Full LES spectra in the middle range of frequencies.

Response: Yes, exactly. This point is addressed in Comment 11, where we provide an illustrative example comparing MAE and PSD at a single grid location at hub height.

Comment 14: "...having a high number of spatially distributed inputs". I think this is the real takeaway from Section 3.2 and 3.4—uniform information density across the domain is key. The more information you have to estimate the flow field (good coverage over the reconstruction area, minimal gaps or distance between useful bits of information) the better. This itself is not surprising, and there should be a good way of describing or estimating analytically the tradeoffs between the number of scans used, the value of interpolation, and the lidar beam half angle.

Response: We agree that a key outcome of Sects. 3.2–3.4 is that a more uniform information density across the rotor plane improves inflow estimation for the proposed methodologies (see Sect. 3.3 and the trends in Sect. 3.4).

To make the associated tradeoffs clearer, we added **Appendix D: Parameter sensitivity of the reconstruction methods**, which presents heat maps of $\text{MAE}_{\text{global}}$ versus θ and n_{scan} for all methods, and versus K for the POD-based methods. An explicit reference to Appendix D has been added in Sect. 3.4 (paragraph 525).

Developing a general analytical descriptor of the tradeoffs between scan count, interpolation, and half-cone angle is valuable but nontrivial for a hub-lidar due to the sampling pattern and the coupled effects of filtering and measurement uncertainty; we therefore document these sensitivities empirically.

Comment 15: Future work. As a final suggestion, for future work it would be great to use this framework to describe the lidar measurement or scanning strategies to minimize error on the estimated inflow, or even better, in terms of granting control authority to the LAC system.

Response: We have incorporated it into the future work discussion in Sect. 5 (paragraph 650).

Comments Referee # 2

Comment 16: There is only one smaller point: It is not clear to me, what is the benefit of using 6 beams measuring with B1 to B6 at [0,240,120,240,120,0] deg over using 3 beams measuring with B1, B2, B3, B2, B3, B1, resulting in measurements at the same location. Further, it is not clear, how the selection of the beam location and order impact the results of the proposed methods. I guess that it would be too much to additionally include the scan order into the parameter sensibility study, but it would be helpful to explain in a bit more detail, how "This azimuthal configuration ensures optimal coverage of the rotor area".

Response: Yes, this is correct. There is no difference between the selected six-beam lidar configuration and a three-beam, as far it follows the selected sequence: B1, B2, B3, B2, B3, B1.

The number of beams and their mounting azimuthal angles ψ_k determine where the hub-lidar samples the rotor plane at each sampling step and thus govern the spatial distribution of measurements available to the reconstruction methods. As discussed in Sects. 3.2–3.4, spatial distribution is a key driver of reconstruction accuracy, particularly for POD–LSQ.

To illustrate how beam location and order impact the results, Fig. 4 compares the sampling pattern over one rotor revolution at $\omega = 9.6$ rpm (or over 6.25 s) for two configurations: Configuration 1 with $\psi = [0°, 240°, 120°, 240°, 120°, 0°]$ (same as in the study) and Configuration 2 with $\psi = [0°, 240°, 120°]$. The remaining parameters are the same as in the study ($t_s = 0.2$ s per beam with no switching delay, range gates from 70 to 350 m with 10 m spacing, and $\theta = 20°$ for all beams). The resulting sampling patterns differ: Configuration 2 leads to clustered consecutive samples and leaves sectors of the rotor disk without measurements, whereas Configuration 1 yields a more spatially distributed pattern. This improved spatial distribution enhances reconstruction performance, even though the same number of samples is projected onto the reconstruction plane.

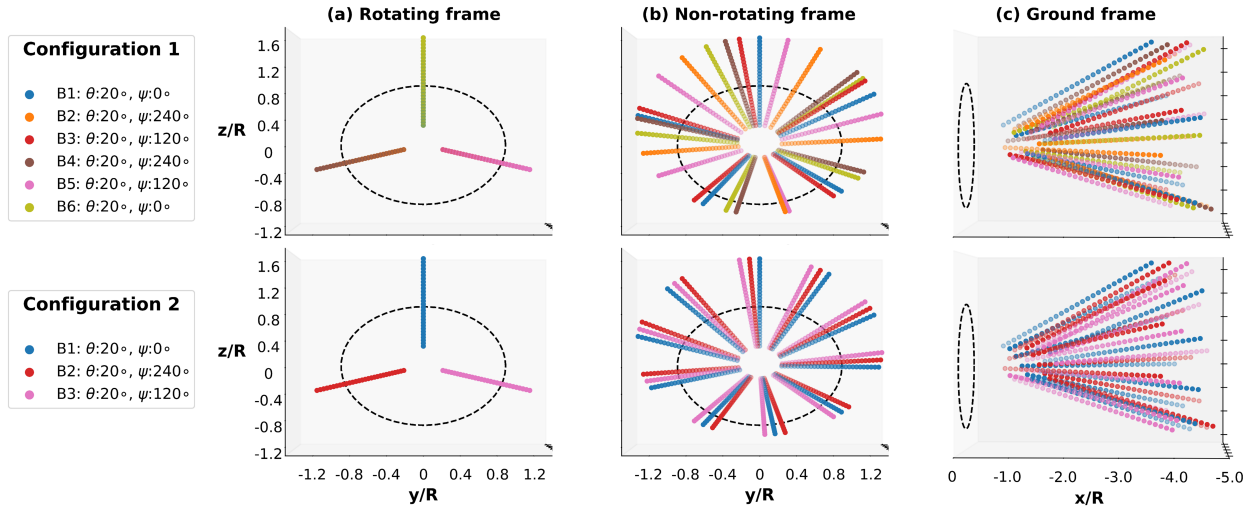

Figure 4: Impact of the azimuthal-angle sequence on the spatial distribution of measurements over one rotor revolution for the DTU 10MW RWT.

Therefore, identifying an azimuthal-angle configuration that provides good spatial coverage across operating conditions depends on the rotor speed and the selected beam

firing sequence. In this study, we determined the configuration by performing an exhaustive search at a fixed rotor speed using `Python`. We prioritize rated and above-rated operation because three of the four inflow cases fall in this regime and LAC applications typically target these conditions. As the referee noted, explicitly including the azimuthal-angle configuration as an additional parameter in the analysis would substantially increase the number of required simulations and is therefore beyond the scope of the present study.

Comment 17: Figure 2: Very helpful figure! You could add the "wind speed quantity" in the last block as "best-performance case selection for each wind speed quantity", or simply remove it from the figure. Further, it might be good to always refer to "wind speed quantity": sometimes it is "wind quantity" (Sec. 3.4) or "wind speed input" and it took me some time to understand that this is the same selection.

Response: We have modified Fig. 2 to include the wind speed quantity analysis in the final block, and we have revised the wording throughout to use "wind speed quantity," including in Fig. 2 and the subtitle in Sect. 3.4.

Comment 18: Figure 3 (c): the green x-axis is pointing upwind, but the values in the x ticks are negative.

Response: We have updated Fig. 3(c) and corrected the x-axis error.

Comment 19: Figure 4: using equal aspect ratio for each axis might help to get a better impression of the scan, c) is not fully projected.

Response: We have improved the aspect ratio of Fig. 4 to enhance readability, and we have changed the description of Fig. 4c. In addition, we corrected a labeling error: the range gates are 70–350 m (not 75–355 m, as previously stated).

Comment 20: Figure 4/5/9: Would be nice to add the radius of the DTU10MW somewhere in the text or figure captions.

Response: We have added the DTU 10MW rotor radius to the captions of these three figures for clarity.

Comment 21: l34f: "Therefore, pulsed lidars exhibit higher coherence with the rotor-effective wind speed (REWS)" This statement needs some refinement from my perspective. As pointed out in Simley et al 2018, standard circular scanning cw lidar usually have a larger coherence bandwidth compared to 4-beam pulsed lidar systems, both performing a scan in 1 second.

Response: We have revised the paragraph in Sect. 1 (paragraph 35) to clarify the advantages of a pulsed lidar system in the context of this study and have removed the previous statement.

Comment 22: l170f: "…only the longitudinal u-component can be estimated from the LOS…". Maybe it would be good to rephrase this: Usually, also other components are estimated from nacelle-based lidar systems (e.g. u and v). How I understood it: the "dilemma" is that you cannot be sure, what is really true.

Response: We have revised the sentence to clarify that two approaches can be used to address the "cyclops dilemma": (i) assuming that the flow sampled by multiple beams is homogeneous, which enables estimation of the u- and v-components, or (ii) assuming a

known wind direction (e.g., aligned with the u-axis) and neglecting the lateral and vertical components. Because the goal of this study is to resolve wind speed variations across the full rotor plane, the second assumption is the most appropriate in this context. The revised text is now included in Sect. 2.3 (paragraph 180).

Comment 23: Equation 5, l270: Z_hub in equation (italic) looks different from the one in the text before the equation and different from the one in l270 (lower case).

Response: We have updated this to reflect the notation used in Eq. 5, using z_{hub}.

Comment 24: Based on equation 5, the origin of the lidar should be impacted by the cos and sin of the shaft length.

Response: Thank you for bringing this to our attention. We did not state this clearly in the original manuscript. The sentence "The measurement point **P** is located at a distance $\overline{OP}$ from the lidar origin **O**, placed at $(-L_s, 0, Z_{\text{hub}})$, where L_s is the shaft length and Z_{hub} the hub height" was misleading.

In our set-up, the lidar origin **O** is located at the hub and has coordinates $(-L_s, 0, Z_{\text{hub}})$. However, the measurement location **P**, is expressed in the (left-handed) global coordinate system whose origin is at the tower base; **P** is therefore defined in that frame as given in Eq. 5.

The projection of V_{LOS} onto the longitudinal direction is performed with respect to the lidar origin **O** and depends only on the hub rotation matrix $\mathbf{R}_{\text{hub}}$. Accordingly, this projection is governed by the beam orientation in the hub frame rather than by the absolute hub position (or shaft length).

We have corrected the text in Sect. 2.4 to express this clearly and moved the lidar origin **O** in Fig. 3(b) to clearly indicate that the origin is located at the hub, not at the tower-top center.

Comment 25: Punctuation after equations: (6,13) period missing, (7) period instead of comma, (8) comma missing.

Response: We have corrected missing periods and commas in Eqs. 6, 7, 8, and 13.

Comment 26: l244 / Figure 5: the lateral and vertical dimensions in Figure 5 look more like the dimensions from box B (which would make sense, since you are interested in rotor-averaged quantities). Maybe it is a typo. But if you used the dimensions of box A (width/height 1.7 rotor diameter), it would be good to adjust the figures.

Response: The figures reflect the dimensions of set B, since it reflect the dimensions of the reconstructed inflows, which match the dimensions of the POD modes. Set A is only used in HAWC2 to extract the lidar data, ensuring full inclusion of lidar probe volume effects. This is mentioned in Sect. 2.7: "Reconstructions are performed on a fixed 39 × 91 grid (y × z), consistent with the global POD modes (Sect. 2.2)".

Comment 27: l272: is it the number of points within A_R and the cuboid?

Response: No, it refers to the number of measurements within the circular region A_R in the fixed YZ plane (Sect. 2.6; Fig. 5c). The total number of measurements in the fixed plane and in the cuboid is not necessarily the same because, as described in Sect. 2.6, if two or more measurements map to the same grid location, only the measurement nearest to the reconstruction plane is retained and the others are discarded. Consequently, the number of measurements available at each time step satisfies $n_{\text{meas},A_R} \leq n_{\text{meas,cuboid}}$. We

have added clarification in Sect. 2.7.1 (paragraph 290).

Comment 28: l276, Figure C1: “lidar” here italic, before normal font.

Response: We have corrected the formatting to be consistent with the rest of the manuscript.

Comment 29: l304: $\times$missing for dimensions?

Response: We have corrected the missing $\times$ into $\boldsymbol{D}_{\mathrm{IDW}} \in \mathbb{R}^{\mathrm{N}_y \times \mathrm{N}_z}$, in Sect. 2.7.4.

Comment 30: l332: you could add 17 x 8 x 10 = 1360 to help the reader to understand where this number is coming from.

Response: We have added this in Sect. 2.8 (paragraph 350).

Comment 31: l359, caption Figure 9: U looks different from before (overline covering not only U?).

Response: We have corrected the mean wind speed notation in the caption of Fig. 9 and also across the manuscript to be consistent, using $\bar{U}_o$.

Comment 32: l379 “)” missing?

Response: We have added the missing parenthesis in Sect. 3.2.

Comment 33: l496: baseline errors are smaller than errors of POD LSQ for small/large angles, so they are not always “highest”.

Response: Thank you for pointing this out. We agree that the original statement was too absolute. We have revised the text at Sect. 3.4 (paragraph 525) to reflect that while the baseline typically yields among the largest errors overall, POD–LSQ can exhibit larger errors than the baseline for extreme half-cone angles.

Comment 34: l515: the probe volume effects are not really accounted for in the wind field reconstruction, but in the lidar simulation… how it is phrased here one might think, lidar users have a choice.

Response: We have revised the phrasing in Sect. 3.4 (paragraph 540) and removed the potentially misleading sentence to avoid misunderstanding.

Comment 35: l638, caption Figure C1: Unit m is in italic.

Response: We have revised the caption of Fig. C1 and corrected the italic formatting and units throughout.

Comment 36: l653: “target” in italic, before normal font.

Response: We have corrected the formatting of “target” in Appendix C.

References

Hauke Beck and Martin Kühn. Temporal up-sampling of planar long-range doppler lidar wind speed measurements using space-time conversion. *Remote Sensing*, 11(7):867, 2019. ISSN 2072-4292. doi: 10.3390/rs11070867. URL https://doi.org/10.3390/rs11070867.

J. F. Céspedes Moreno, J. P. Murcia León, and S. J. Andersen. Convergence and efficiency of global bases using proper orthogonal decomposition for capturing wind turbine wake aerodynamics. *Wind Energ. Sci.*, 10(3):597–611, 2025. doi: 10.5194/wes-10-597-2025. URL https://wes.copernicus.org/articles/10/597/2025/.

M. Gräfe, V. Pettas, J. Gottschall, and P. W. Cheng. Quantification and correction of motion influence for nacelle-based lidar systems on floating wind turbines. *Wind Energ. Sci.*, 8(6):925–946, 2023. doi: 10.5194/wes-8-925-2023. URL https://wes.copernicus.org/articles/8/925/2023/.

Azur Hodzic, Peder Olesen, and Clara Velte. On the discrepancies between pod and fourier modes on aperiodic domains. *Journal of Engineering Mathematics*, 145, 03 2024. doi: 10.1007/s10665-024-10340-8.

M. Kelly and M. P. van der Laan. From shear to veer: theory, statistics, and practical application. *Wind Energy Science*, 8(6):975–998, 2023. doi: 10.5194/wes-8-975-2023. URL https://wes.copernicus.org/articles/8/975/2023/.

J. L. Lumley. The structure of inhomogeneous turbulence. In *Atmospheric Turbulence and Wave Propagation*, pages 166–178. Nauka, Moscow, 1967. ISBN 9783937655239.

David Schlipf. *Lidar-Assisted Control Concepts for Wind Turbines*. Ph.d. thesis, University of Stuttgart, Institute of Aircraft Design, University of Stuttgart, 2016. URL http://dx.doi.org/10.18419/opus-8796.

Wind-field estimation for lidar-assisted control: A comparison of proper orthogonal decomposition and interpolation techniques

Esperanza Soto Sagredo[1], Søren Juhl Andersen[1], Ásta Hannesdóttir[1], and Jennifer Marie Rinker[1]
[1]Department of Wind and Energy Systems, Technical University of Denmark, Denmark
Correspondence: Esperanza Soto Sagredo (espa@dtu.dk)

Abstract.

This study presents and evaluates three wind field reconstruction methods for real-time inflow characterization, with potential applications in lidar-assisted wind turbine control. The first method applies a least-squares fit of proper orthogonal decomposition (POD) modes to lidar measurements (POD-LSQ). The second uses inverse distance weighting (IDW) interpolation across the rotor plane. The third, POD-IDW, applies the POD-LSQ fit to the interpolated field. The methods are tested under semi-realistic conditions derived from large-eddy simulations (LES), using a hub-mounted lidar sensor implemented in HAWC2 on the DTU 10 MW reference turbine. Measurements are extracted under varying inflow conditions. A rotor-effective wind speed estimate, combined with the known vertical shear profile from LES, serves as the baseline for comparison. Reconstruction performance is quantified using a global mean absolute error, evaluated across combinations of scan count, POD mode number, and lidar beam angle. Optimal parameters are selected based on the minimum error. To assess physical accuracy, reconstructions are compared against true wind speeds, evaluating the effects of probe volume averaging, multi-distance measurement selection, cross-contamination, and other sources of error. For optimal inputs, POD-IDW achieves the highest accuracy, reducing error by 45.5% compared with the baseline estimation, at 5.4 times the computational cost. IDW performs similarly (44.9%) with optimal inputs, while POD-LSQ achieves a 39.4% reduction with minimal overhead (7%). Spectral analysis shows that volume averaging and scanning strategies introduce low-pass filtering that attenuates high-frequency turbulence, while preserving low-frequency content more accurately than the baseline. Reconstruction quality strongly depends on the number and spatial distribution of lidar measurements and the number of retained POD modes. Although demonstrated under idealized conditions, the methods show strong potential for real-time applications. Future work should integrate these reconstructions with flow-aware controllers to evaluate fatigue load reduction, particularly at tower level.

1 Introduction

The upscaling of wind turbines has led to increasingly large and flexible rotors. While larger rotors average out small-scale fluctuations, they also increase sensitivity to spatio-temporal wind variability, which impacts both power production and structural loading (Angelou and Sjöholm, 2022). To mitigate these effects, advanced control strategies are needed to enhance performance while minimizing fatigue and extreme loads (Dong et al., 2021; Angelou and Sjöholm, 2022; Russell et al., 2024).

Lidar-assisted control (LAC) has emerged as a promising approach to reduce fatigue loads (Bossanyi et al., 2012; Guo et al., 2023; Fu et al., 2023; Russell et al., 2024), extreme loads (Schlipf and Kühn, 2008), and the levelized cost of energy (Scholbrock et al., 2016; Simley et al., 2018). Conventional LAC systems use nacelle-mounted lidars, which measure upstream wind via Doppler sensing and enable feedforward control by anticipating turbulence (Bossanyi et al., 2012; Schlipf et al., 2015; Simley et al., 2018). However, nacelle-mounted lidars performance is hindered by blade blockage, causing data loss and increased uncertainty in wind field estimation (Schlipf et al., 2018; Angelou and Sjöholm, 2022). Mounting the lidar on the hub or spinner (hereafter hub-lidar) mitigates blockage and improves scan availability.

While hub mounting addresses the geometric source of data loss, data availability and reconstruction fidelity are also shaped by the lidar measurement principle itself. Continuous-wave (CW) lidars measure wind speed at a single focus distance through a range-weighted probe volume, whereas pulsed lidars use range gating to retrieve velocities at multiple distances along the line-of-sight (LOS) (Peña et al., 2015); however, this broader spatial coverage is typically achieved at the expense of longer effective sampling times than CW systems (Letizia et al., 2023). Building upon the blockage mitigation provided by hub mounting, a pulsed hub-lidar combines multi-range, longer-range measurements with improved scan availability, thereby providing spatially distributed inflow observations that are well suited for wind-field reconstruction and subsequent LAC feedforward control, depending on appropriate lidar configuration selection.

Among LAC strategies, feedforward collective pitch control is the most established. It adjusts all blades simultaneously by using REWS estimated as the averaged wind velocities measured by the lidar and projected into the longitudinal direction (Held and Mann, 2019), improving rotor speed regulation and reducing loads (Dunne et al., 2011; Canet et al., 2021; Fu et al., 2023). However, reliance on spatially averaged REWS becomes less valid as rotor size increases.

To address this, feedforward individual pitch control adjusts each blade independently in response to localized wind. Approaches include combining REWS with horizontal and vertical shear profiles (Schlipf et al., 2010; Dunne et al., 2012) or measuring blade-level wind speeds at fixed radial and azimuthal positions (Dunne et al., 2012; Russell et al., 2024). Despite their benefits, these methods rely on simplified inflow assumptions and do not resolve spatio-temporal structures, which become increasingly inadequate for large rotor diameters. Thus, there is a critical need for real-time, high-fidelity wind field reconstruction algorithms capable of resolving the spatial and temporal structures of the incoming wind, enabling more advanced LAC strategies and improved load mitigation across both tower and blade components.

High-fidelity reconstruction methods are therefore needed to capture the full wind field dynamics. Spectral techniques (Dimitrov and Natarajan, 2016; Rinker, 2022; Fu et al., 2022; Guo et al., 2022), CFD-based optimization (Bauweraerts and Meyers, 2021), and Bayesian estimation (Bauweraerts and Meyers, 2020) exist but are computationally intensive and not suited for real-time applications. Physics-informed machine learning approaches show promise for fast inflow reconstruction (Zhang and Zhao, 2021a, b), but lack demonstrated scalability for utility-scale turbines.

Proper orthogonal decomposition (POD) offers a computationally efficient model reduction technique by decomposing velocity fields into spatial modes and time-dependent coefficients that capture the flow's temporal evolution. It has been used in wind energy to study turbine wakes for individual flow cases (VerHulst and Meneveau, 2014; Newman et al., 2014; Andersen et al., 2017; De Cillis et al., 2020). While early POD applications lacked predictive generality (Meneveau, 2019),

Andersen and Murcia Leon (2022) introduced a global POD basis by combining multiple flow cases, allowing the basis to span a broader parameter space and enabling consistent physical interpretation across different flow conditions. More recently, Céspedes Moreno et al. (2025) evaluated the performance of a global basis in reconstructing wake aerodynamics, showing that the reconstruction error decreases and converges as more cases are included in the dataset.

Focusing now on the use of lidar measurements in combination with POD, recent studies have explored both wake characterization and inflow reconstruction. In the context of wakes, Hamilton et al. (2025) applied POD to horizontal scans from nacelle-mounted lidars to identify coherent turbulent structures experienced by a turbine operating in the wake of an upstream rotor. For inflow reconstruction, Sekar et al. (2022); Kidambi Sekar et al. (2022) combined SpinnerLidar measurements with POD to estimate the incoming turbulent wind field. However, their approach relies on a complex and non-commercial lidar system (Mikkelsen et al., 2013; Herges et al., 2017), and it requires prior knowledge of the inflow, limiting its predictive capability. To address these limitations, Soto Sagredo et al. (2024a) proposed a least-squares fit of POD (POD-LSQ) method using hub-lidar data to estimate modal amplitudes in real time without requiring prior flow information. While promising, this approach was developed using idealized Mann-generated turbulence (Mann, 1998), and its robustness under realistic inflow conditions remains to be demonstrated.

Interpolation offers another approach for inflow reconstruction. Techniques such as kriging, inverse distance weighting (IDW), and cokriging are widely used in meteorology to estimate wind from sparse data (Luo et al., 2007; Joyner et al., 2015; Friedland et al., 2016). Similar methods have been applied to lidar-based wind field reconstruction (Chu et al., 2021; Bao et al., 2022), though they struggle to resolve unsteady 3D flow structures due to limited coverage and assumptions. In a related context, Beck and Kühn (2019) developed a space-time conversion method for planar long-range Doppler lidar measurements, employing spatial interpolation as part of a temporal up-sampling framework for wind turbine wake fields; while their focus is on correcting scan-inherent time shifts rather than inflow reconstruction, the work illustrates the broader role that interpolation schemes play in recovering wind field information from spatially and temporally sparse lidar data. Particularly, IDW is a widely used interpolation technique in geosciences, environmental science, and spatial data analysis (Bokati et al., 2022), and was also used by Soto Sagredo et al. (2024b) to reconstruct rotor-plane wind fields using hub-lidar data. While promising for real-time use, that study focused on idealized conditions and a single wind speed.

This study addresses the need for robust, real-time wind field reconstruction under varying inflow conditions. We evaluate three techniques: POD-LSQ, IDW, and a hybrid POD-IDW approach, comparing them against a REWS-based baseline that includes the vertical shear profile. Using LES-generated inflow and a numerical six-beam pulsed hub-lidar, we assess reconstruction accuracy and sensitivity to different input parameters across methods and inflow conditions. In particular, POD-LSQ shows promise for LAC due to its computational efficiency and spatial fidelity.

The paper is structured as follows: Section 2 describes the methodology, including LES inflow, lidar setup, and reconstruction methods. Section 3 evaluates the performance of each method across varying inflow conditions, analyzing their sensitivity to input parameters and measurement uncertainty to identify the optimal parameter combinations for each reconstruction approach. Section 4 discusses implications and limitations, while section 5 concludes the paper and outlines future work.

2 Methodology

To evaluate the wind field estimation techniques, synthetic lidar data are generated using high-fidelity inflow conditions from LES and a numerical hub-lidar sensor implemented on the DTU 10 MW reference wind turbine (RWT) model (Bak et al., 2013) in HAWC2 v13.1 (DTU Wind Energy, 2024), which includes a flexible tower and a five degree tilt. The methodology is first summarized in the following paragraphs before being described in detail in the subsequent subsections.

An overview of the wind field reconstruction concept using pulsed hub-lidar technology is shown in Fig. 1. The multi-distance projected LOS velocities captured by the hub-lidar are mapped onto a reconstruction plane, where an estimation method reconstructs the spatio-temporal wind field. This high-resolution inflow can potentially support advanced control strategies by enabling real-time adaptation to turbulent structures and improving load mitigation.

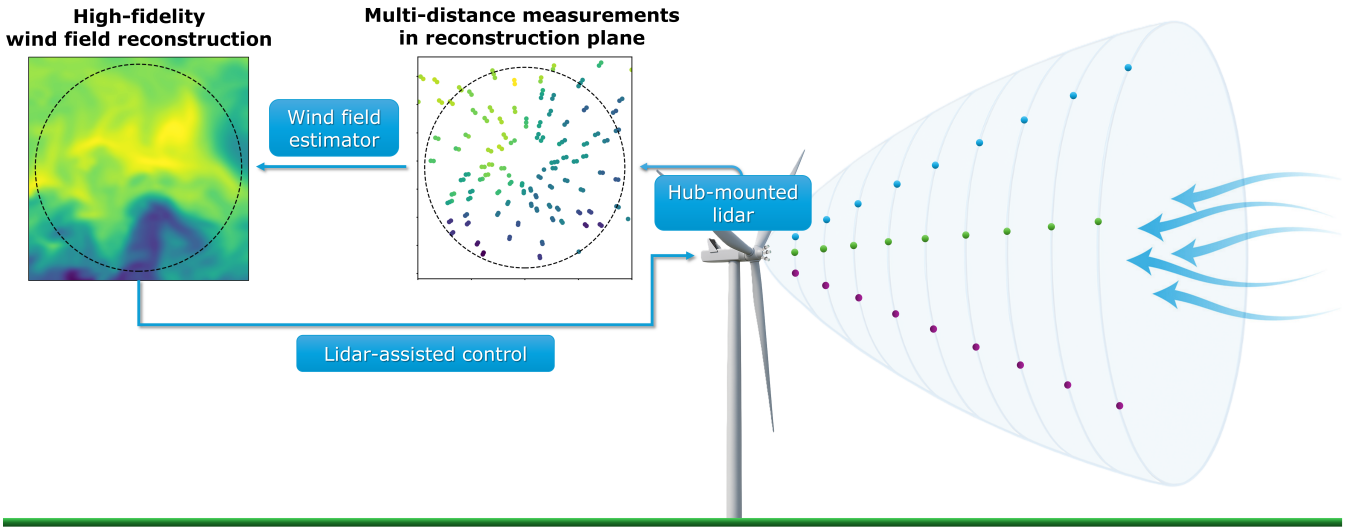

Figure 1. Schematic overview of the wind field reconstruction approach used in this study, using pulsed hub-lidar measurements for LAC.

Figure 2 outlines the numerical framework used to assess each method's accuracy. The primary goal is to quantify reconstruction error and analyze sensitivity to key input parameters: the lidar beam half-cone angle (θ), the number of scans (n_{scan}), the number of POD modes used for truncation (K), and the influence of measurement uncertainty.

The process begins with a turbulence database derived from LES inflow fields, divided into two subsets: Set A is used to extract hub-lidar measurements in HAWC2, serving as the reference dataset, while set B is used to construct the global POD basis. After preprocessing, the lidar data are mapped to the reconstruction plane and decomposed into wind fluctuations in the YZ-plane, which are then used as inputs to the reconstruction methods. The reconstructed fields are compared against the reference fields to compute the reconstruction error, where the best-performing cases across multiple inflow conditions are identified by selecting the parameter combinations that yield the lowest error. This systematic framework enables a

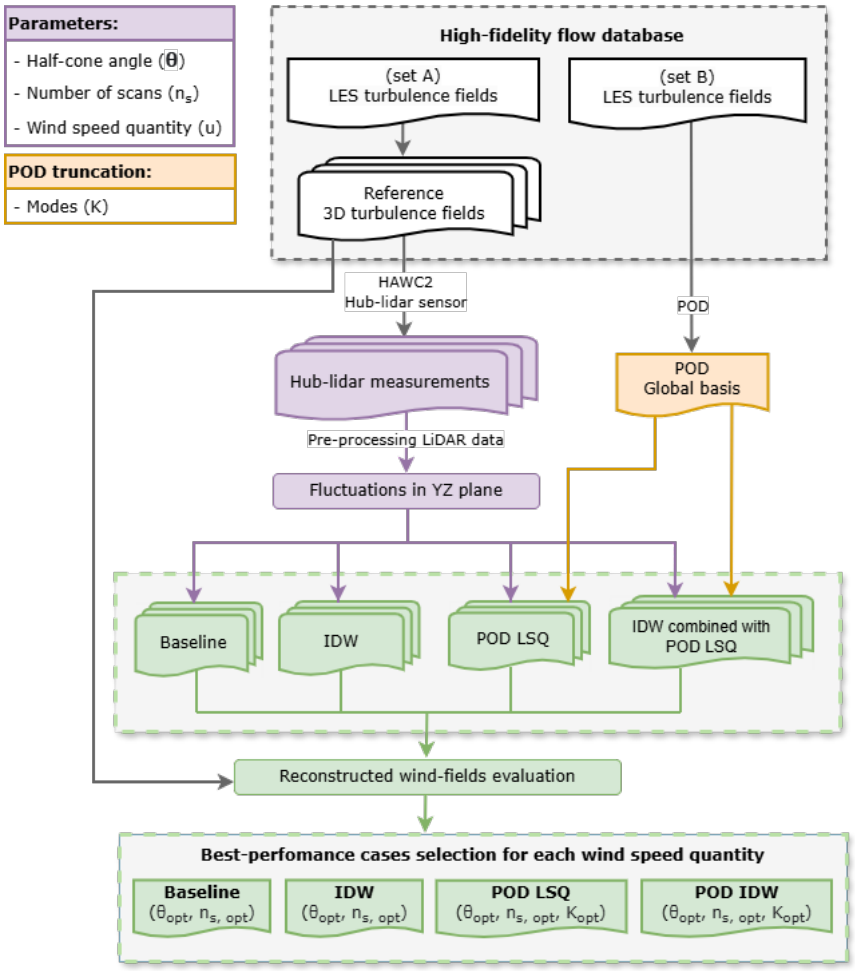

Figure 2. Numerical framework for wind field reconstruction evaluation using synthetic lidar measurements and four reconstruction techniques.

consistent evaluation of each method and supports the identification of robust configurations suitable for real-time wind field reconstruction.

2.1 LES precursor

The LES data used in this study originates from precursor simulations by Andersen and Murcia Leon (2022).

The precursor simulates a neutral atmospheric boundary layer driven by a steady pressure gradient over flat terrain. It is performed using the EllipSys3D flow solver (Michelsen, 1992, 1994; Sørensen, 1995), which solves the Navier–Stokes equations in general curvilinear coordinates using a finite volume method on a block-structured and collocated grid.

The computational domain spans 2880 m $\times$ 1440 m $\times$ 700.8 m, discretized into $576 \times 288 \times 320$ cells, with uniform grid spacing of 5 m in the longitudinal and lateral directions and 2.19 m vertically. To avoid spanwise locking of turbulent structures, a lateral shift is applied to the periodic boundaries in the longitudinal direction, following Munters et al. (2016). The simulation assumes a surface roughness of $z_0^{\mathrm{org}} = 0.05$ m and a friction velocity of $u_*^{\mathrm{org}} = 0.4545$ m s^{-1}. It runs for 82,600 s (approximately 22.94 h) to ensure statistical convergence before collecting 28,800 s of inflow data.

As described by Castro (2007), neutral atmospheric boundary flows can be rescaled to generate multiple inflow conditions. We apply this rescaling following Troldborg et al. (2022):

$$u^{\mathrm{new}} = u_*^{\mathrm{new}} \left(\frac{u^{\mathrm{org}}}{u_*^{\mathrm{org}}} + \frac{1}{\kappa} \ln \frac{z_0^{\mathrm{org}}}{z_0^{\mathrm{new}}} \right), \tag{1}$$

where $\kappa = 0.41$ is the von Kármán constant, and the superscript "new" refers to the inflow condition to be generated, where $u^{\mathrm{new}} \in [8.0, 12.0, 15.0, 18.0]$ m s^{-1}, obtaining four inflow wind speeds. All inflows have an average TI of approximately 11%.

2.2 LES datasets

The LES datasets (set A and B) are taken from two different locations within the LES domain and have distinct spatial dimensions in the lateral and vertical directions. Set A consists of $28800 \times 1 \times 61 \times 138$ grid points ($t \times x \times y \times z$), while set B includes $28800 \times 1 \times 39 \times 91$ grid points. Both datasets cover a 4-hour period at a temporal resolution of $d_t = 0.5$ s, with spatial resolutions of 5 m in the lateral (y) direction and 2.19 m in the vertical (z) direction. An illustration of the locations in the LES domains is given in Fig. A in the appendix for clarity. For each inflow wind speed, the three turbulent velocity components (u, v, w) are extracted and rescaled following the method described in Sect. 2.1.

To ensure that the global POD basis characterizes the coherent turbulent structures over the rotor area, the spatial domain of set B is reduced and centered accordingly, spanning 190.3×197.1 m ($y \times z$). In contrast, set A retains a larger spatial extent of 300.5×300.0 m ($y \times z$), providing sufficient coverage for aeroelastic simulation and lidar probe volume modeling.

From set A, sixteen non-overlapping 900 s segments are extracted to generate sixteen independent 3D turbulent inflow fields. These are transformed into spatial boxes under Taylor's frozen turbulence hypothesis (Taylor, 1938), which assumes that turbulent structures are convected downstream at a constant advection velocity $\bar{U}_o$—the average wind speed at hub height—without evolving in time. Under this transformation, the time and longitudinal directions are combined to define the longitudinal coordinate x, with a spatial resolution given by:

$$d_x = \frac{\bar{U}_o T_{\mathrm{sim}}}{N_x}, \quad \text{where } N_x = \frac{T_{\mathrm{sim}}}{d_t} = 1800, \quad T_{\mathrm{sim}} = 900 \text{ s}.$$

The resulting reference turbulence boxes have dimensions of $1800 \times 61 \times 138$ grid points ($x \times y \times z$), enabling accurate 15-minute HAWC2 simulations and ensuring full inclusion of lidar probe volume effects.

To account for HAWC2's transient effects, lidar initialization and boundary effects, the first 250 s and the last 50 s of the simulation are discarded—beyond the conventional 100 s warm-up typically used in HAWC2—yielding the final reconstructed wind fields of 600 s, with dimensions of $1200 \times 39 \times 91$ grid points ($t \times y \times z$), with a time step $d_t = 0.5$ s.

2.3 Proper orthogonal decomposition and global basis

POD decomposes turbulent flow into orthogonal spatial modes that optimally capture the variance of the fluctuations (Lumley, 1967; Berkooz et al., 1993). Typically, POD is applied to a single flow case, yielding an orthogonal basis optimized for that specific dataset.

To enable generalization across different flow conditions, Andersen and Murcia Leon (2022) utilized a "global" POD basis, which is derived by combining multiple cases, providing a more general representation across a broader parameter space. As the global POD modes are derived from multiple flow conditions, they are not optimized for any single case but instead capture generalized flow structures across the parameter space. However, as shown by Céspedes Moreno et al. (2025) the global basis is still very effective and the suboptimality of a global basis compared to a "local" basis is at least an order of magnitude smaller than the truncation error.

To compute the basis, we first calculate the fluctuating component of the longitudinal velocity field by subtracting the temporal mean, $\bar{U}(y,z)$, from the full velocity field: $\boldsymbol{U}'(y,z,t) = \boldsymbol{U}(y,z,t) - \bar{\boldsymbol{U}}(y,z)$. These fluctuations are then reshaped into column vectors over N_t time steps for each of N_c flow cases, forming the matrix $\mathbf{M} = [\boldsymbol{U}'_{1,1}, \ldots, \boldsymbol{U}'_{1,\mathrm{N_t}}, \ldots, \boldsymbol{U}'_{\mathrm{N_c},1}, \ldots, \boldsymbol{U}'_{\mathrm{N_c},\mathrm{N_t}}]$, which is used to compute the POD modes using the randomized singular value decomposition (SVD) following the method of Halko et al. (2011).

The decomposition yields a set of orthonormal spatial modes $\mathbf{G} = [\boldsymbol{g}_1, \ldots, \boldsymbol{g}_{\mathrm{N_t}-1}]$. A visualization of the first ten global POD modes is provided in Appendix B.

The corresponding modal time series are obtained by projecting the fluctuating flow onto the spatial POD modes using an inner product $\phi_i(t) = \langle \boldsymbol{U}'(t), \boldsymbol{g}_i \rangle$.

A reduced-order approximation of the flow field can then be constructed as:

$$\boldsymbol{U}(y,z,t) = \sum_{i=1}^{K} \boldsymbol{g}_i(y,z)\,\phi_i(t) + \bar{U}(y,z) \tag{2}$$

where $K < N_t - 1$ is the number of retained modes and $\phi_i(t)$ are the modal time coefficients. This approach provides a low-dimensional representation of the flow, retaining dominant coherent structures while reducing computational complexity.

Although accurate representation of the flow physics in POD requires all three velocity components (u, v, w) (Iqbal and Thomas, 2007), in this study we only extract the global POD modes using the longitudinal component (u) from the LES dataset set B (see Sect. 2.2). This choice reflects the focus on reconstructing the longitudinal wind speed, which is the primary quantity of interest for LAC applications. The simplification is motivated by both methodological and practical considerations. First, u-component fluctuations dominate turbine loads (Dimitrov et al., 2018), whereas lateral (v) and vertical (w) components have negligible impact (Dimitrov and Natarajan, 2016). Additionally, only the longitudinal u-component can be estimated from the LOS. This limitation arises because the lidar does not measure the full three-dimensional velocity vector; instead, it senses only the component projected along the beam direction (the “cyclops dilemma”) (Raach et al., 2014). Recovering individual velocity components from LOS measurements therefore requires additional assumptions. One option is to combine multiple beams under an assumption of local flow homogeneity (Sathe et al., 2015), which enables estimation of multiple velocity

components (e.g., u, v, and/or w) but relies on limited spatial variability across the rotor. A second approach is to assume a known wind direction (e.g., align with the u-component) and neglect the lateral and vertical components (Letizia et al., 2023). Because this study aims to resolve wind speed variations across the full rotor plane, we adopt the latter assumption, and thus estimate only the longitudinal component u from the LOS measurements.

To avoid data leakage and promote generalization, the POD basis is computed from LES domains that are spatially offset from the reconstruction region (Appendix A).

2.4 Numerical lidar sensor

A numerical model of a hub-mounted pulsed lidar sensor is available in HAWC2 v13.1 (Soto Sagredo et al., 2023) to simulate realistic LOS wind measurements based on user-defined parameters for a single-beam lidar. This section outlines the sensor used in this study, including lidar parameters, coordinate system, and estimation of longitudinal wind speed.

The hub-lidar consists of a pulsed single-beam sensor installed on the spinner and constrained to the wind turbine model, meaning that the lidar beams moves with the turbine structure and is affected by tower motion, including yaw, pitch, roll and structural vibrations. As the spinner rotates, the beam sweeps the rotor area, measuring LOS wind speeds by projecting the local u-, v-, and w-components onto the LOS direction (Fig. 1). Tower motion together with rotor rotation influences the measurements by introducing a relative-velocity contribution to the measured wind speed. However, in the current HAWC2 hub-lidar sensor implementation, rotor rotation does not introduce an additional translational velocity component in the measured wind speed. Motion-induced fluctuations are therefore dominated by tower motion and can be mitigated using frequency-domain filtering, which preserves the integrity of the estimated wind field without introducing bias (Gräfe et al., 2023). In practical deployments, such pre-processing should be applied before reconstructed inflow fields are used for load assessment or LAC, because uncorrected motion artifacts can excite structural dynamics, inflate fatigue loads, and, in control applications, provoke undesirable actuator responses (Schlipf, 2016). Nevertheless, no motion correction or filtering has been applied in the present analysis, because the study focuses on inflow reconstruction accuracy under multiple uncertainty sources.

Probe volume effects are simulated by HAWC2 using the weighting function and system parameters described in Meyer Forsting et al. (2017) for pulsed lidar systems. HAWC2 provides as outputs: (i) the probe volume-averaged LOS velocity $V_{\mathrm{LOS,\,wgh}}$; (ii) the nominal LOS velocity $V_{\mathrm{LOS,\,nom}}$, without volume averaging; and (iii) the corresponding measurement locations in X, Y, Z.

The lidar beam unit directional vector, $\mathbf{n}(\theta, \psi, \omega(t))$, can be defined in a left-handed Cartesian coordinate system, with X downwind and Z vertical direction as:

$$\mathbf{n}(\theta, \psi, \omega(t)) = (-\cos(\theta),\ -\sin(\theta)\sin(\psi + \omega(t)),\ \sin(\theta)\cos(\psi + \omega(t))), \tag{3}$$

where θ is the half-cone angle, ψ the azimuthal offset from blade 1 where the lidar beam is located (clockwise viewed downwind) and $\omega(t)$ is the azimuthal angle of blade 1 (origin aligned with the Z-axis upward, rotation clockwise viewed downwind).

The LOS-velocity (also called radial velocity) can be mathematically expressed as:

$$V_{\mathrm{LOS}}(\theta, \psi, \omega(t), \boldsymbol{P}) = \boldsymbol{n}(\theta, \psi, \omega(t)) \cdot \boldsymbol{U}(\boldsymbol{P}), \tag{4}$$

where $\mathbf{U}(\mathbf{P}) = [u(\mathbf{P}), v(\mathbf{P}), w(\mathbf{P})]^T$ is the wind vector, and $\mathbf{P}$ represents the location in space (x, y, z) where the measurement is taken, as a function of the instantaneous hub location, the lidar beam unit vector and the range length, f_d.

Figure 3 illustrates the beam configuration from three perspectives, for a beam with $\theta = 20°$, $\psi = 30°$, and a range length $f_d = 200$ m, where the spatial location of the measurement point $\mathbf{P}$ is express as:

$$\mathbf{P}(\theta, \psi, \omega(t), \beta, \nu, \gamma, f_d) = \mathbf{R}_{\text{hub}}(\beta, \nu, \gamma) \cdot \begin{bmatrix} -L_s \\ 0 \\ 0 \end{bmatrix} + \begin{bmatrix} 0 \\ 0 \\ Z_{\text{hub}} \end{bmatrix} + \mathbf{R}_{\text{hub}}(\beta, \nu, \gamma) \cdot f_d \cdot \mathbf{n}(\theta, \psi, \omega(t)), \tag{5}$$

where L_s is the shaft length, Z_{hub} the hub height, and $\mathbf{R}_{\text{hub}}(\beta, \nu, \gamma)$ is the rotation matrix accounting for tilt (β), roll (ν), and yaw (γ) of the wind turbine model for a left-handed coordinate system. For this study, $\beta = 5.0°$ and $\nu = \gamma = 0$.

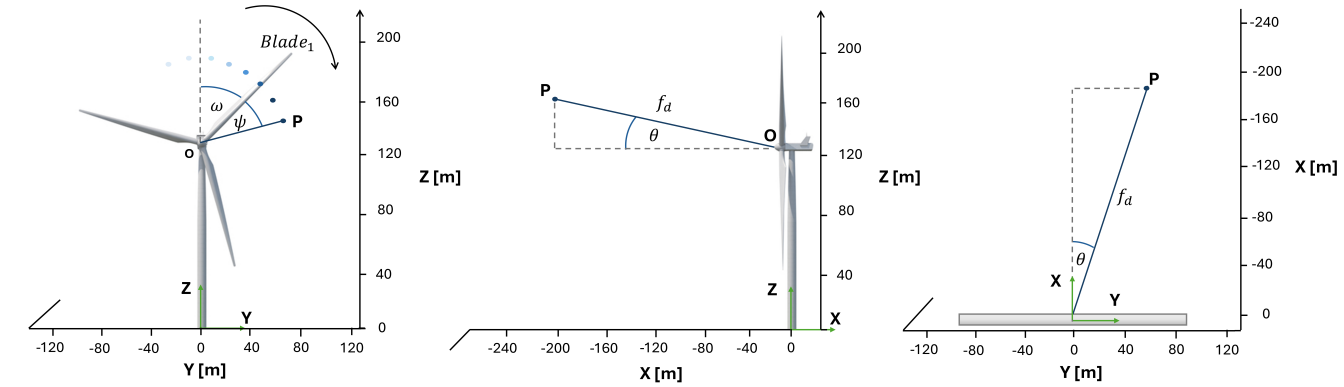

(a) Plane YZ, front view of the wind turbine and single beam lidar looking downwind.

(b) Plane XZ, side view of wind turbine and single beam lidar.

(c) Plane XY, top view of wind turbine and single beam lidar.

Figure 3. Left-handed coordinate system for a single-beam lidar mounted on the DTU 10 MW RWT. Example with range length $f_d = 200$ m, half-cone angle $\theta = 20°$, azimuthal angle $\psi = 30°$, and blade 1 at $\omega = 35°$.

Therefore, the LOS-velocity accounting for beam orientation and tilt can be finally express as:

$$\begin{aligned} V_{\text{LOS}}(\theta, \psi, \omega(t), \beta, \mathbf{P}) = &[\cos(\beta)\cos(\theta) - \sin(\beta)\sin(\theta)\cos(\psi + \omega(t))] \cdot u(\mathbf{P}) + [\sin(\theta)\sin(\psi + \omega(t))] \cdot v(\mathbf{P}) \\ &+ [\sin(\beta)\cos(\theta) + \cos(\beta)\sin(\theta)\cos(\psi + \omega(t))] \cdot w(\mathbf{P}). \end{aligned} \tag{6}$$

The longitudinal wind speed is estimated by projecting V_{LOS} onto the x-axis. This projection assumes negligible lateral and vertical components (v and w) when the rotor is perfectly aligned with the wind (Schlipf et al., 2013; Simley et al., 2011), which introduces cross-contamination errors (Kelberlau and Mann, 2020). The final equation to project the LOS velocity to the longitudinal direction is thus as follows:

$$u_{\text{lidar}}(\theta, \psi, \omega(t), \beta, \mathbf{P}) = \frac{V_{\text{LOS}}(\theta, \psi, \omega(t), \mathbf{P})}{\cos(\beta)\cos(\theta) - \sin(\beta)\sin(\theta)\cos(\psi + \omega(t))}. \tag{7}$$

Noticed that the projection is performed from the lidar origin $\mathbf{O}$, placed at $(-L_s, 0, Z_{\text{hub}})$, and therefore, the projection is only affected by the rotation matrix $\mathbf{R}_{\text{hub}}$.

Effects related to optics, internal signal processing, and lidar-specific smearing are not considered in this study.

2.5 Lidar scanning strategy

The HAWC2 hub-lidar sensor supports flexible scanning configurations, allowing multiple beams with user-defined half-cone angles (θ), azimuthal angles (ψ), and range lengths (f_d). In this study, a six-beam configuration is employed, with each beam sampled sequentially at 5 Hz and no switching delay. The lidar records 29 fixed range gates spaced every 10 m, covering distances from 70 m to 350 m—consistent with common pulsed lidar practice (Peña et al., 2013). During post-processing, the beam sequence, sampling frequency, and switching delay can be customized.

Preliminary analysis (not shown for brevity) revealed that reconstruction accuracy improves when all six lidar beams are angled away from the central axis, rather than having a central beam pointing directly upwind. Although each beam samples multiple range gates, a beam aligned with the wind direction collects data along a nearly straight line, with only a slight vertical shift due to turbine tilt. As a result, many measurements overlap and map into the same grid location, providing only a small number of central points in the fixed spatial grid. In contrast, angled beams increase their spatial coverage and provide more data for the estimation across the rotor plane. Similar results have been reported by Simley et al. (2014), where optimal scan radii was found to be approximately 70-75% of the rotor span.

The half-cone angle selection affects both projection errors—due to the assumption of negligible v and w components—and the spatial coverage of the rotor. Increasing the preview distance reduces cross-contamination and induction effects but increases errors due to wind evolution (Simley et al., 2012). Since HAWC2 does not model induction in the lidar sensor or temporal evolution of inflow, their impact is therefore not considered in this study.

The azimuthal angle defines each beam's angular separation from blade 1 in the rotating frame (Fig. 3), with allowable values in this study, $\psi \in [0°, 120°, 240°]$, based on practical installation constraints. Specifically, for many multi-megawatt wind turbines, manufacturers provide access to the hub through service hatches positioned every 120 degrees. Aligning the lidar beams with these access points simplifies both the installation and maintenance process.

The goal is to optimize the beam sequence to maximize rotor plane coverage over a given number of scans, where a "scan" is defined as the time needed to sample all six beams. At 5 Hz per beam, a single scan takes $t_{\text{scan}} = 1.2$ s.

Figure 4 illustrates the final six-beam hub-lidar configuration, which was found with an exhaustive search through iteration at fixed rotor speed $\Omega = 9.6$ rpm (rated speed of the DTU 10 MW turbine), yielding the optimal beam sequence: $\psi = [0°, 240°, 120°, 240°, 120°, 0°]$. Panel (a) shows the initial mounting azimuthal angles (YZ view), (b) the scanning trajectory over one scan (non-rotating frame), and (c) beam locations ~~projected~~ onto the XZ plane. This azimuthal configuration ensures optimal coverage of the rotor area above rated wind speed, since this is the operational range where LAC is used for load reduction.

2.6 Measurement selection for reconstruction

Synthetic lidar measurements are extracted from the reference inflow fields (Sect. 2.2) using the hub-lidar sensor. During post-processing, the 20 Hz HAWC2 lidar output is downsampled to a 5 Hz sampling rate per beam, with no switching delay.

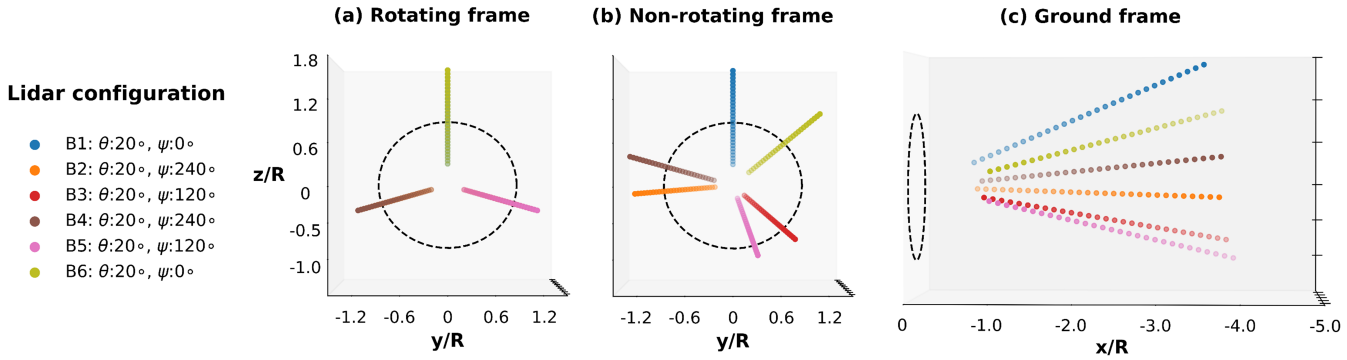

Figure 4. Six-beam lidar configuration with a half-cone angle $\theta = 20°$ for all beams, azimuthal angles $\psi = [0°, 240°, 120°, 240°, 120°, 0°]$, and 29 range-gates from 70 to 350 m spaced every 10 m. (a) Initial beam mounting positions (YZ view); (b) scanning trajectory over one scan at $\Omega = 9.6$ rpm; (c) beam locations ~~projected~~ on the XZ plane. The black dashed circle indicates the DTU 10 MW RWT rotor ($R = 89$ m).

Measurements used for the reconstruction are selected through a spatial filtering process. In the lateral and vertical directions, the filter dimensions match those of the turbulence box from set A (refer to Sect. 2.2). In the longitudinal direction, the filter spans a distance $d_{\text{span}} = \bar{U}_o\, n_{\text{scan}}\, t_{\text{scan}}$, where n_{scan} is the selected number of scans and $t_{\text{scan}} = 1.2$ s is the duration of a single full scan. This longitudinal span is centered around the target reconstruction plane, located at $X_{\text{target}} = \bar{U}_o\, t_s$, where t_s denotes the time step at which the reconstruction is evaluated. As a result, only measurements satisfying the condition $X_{\text{target}} - \frac{1}{2}\bar{U}_o\, n_{\text{scan}}\, t_{\text{scan}} < x < X_{\text{target}} + \frac{1}{2}\bar{U}_o\, n_{\text{scan}}\, t_{\text{scan}}$ are selected for the reconstruction. Additionally, we imposed a constraint requiring all selected measurements to be located at least one second upstream of the rotor plane, to ensure preview time.

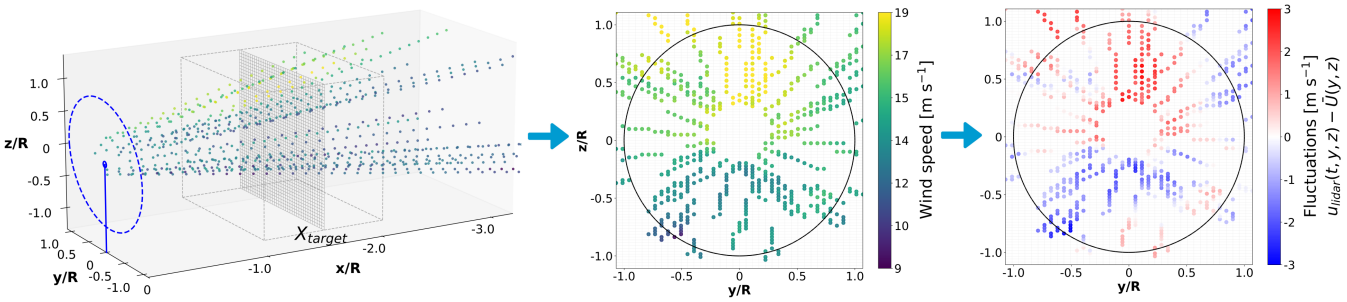

(a) Hub-lidar measurements and target estimation plane for reconstruction.

(b) Selected measurements mapped onto fixed grid in the YZ plane.

(c) Fluctuations mapped onto fixed grid in the YZ plane.

Figure 5. Lidar measurement selection for wind-field reconstruction at a single time step. (a) Lidar data advancing toward the rotor with the spatial filtering cuboid centered at $X_{\text{target}} = \bar{U}_o t_s$. (b) Mapping onto a fixed YZ grid. (c) Subtraction of the vertical wind speed profile. The black dashed circle in plots (b) and (c) indicates the DTU 10 MW RWT rotor ($R = 89$ m).

This process is illustrated in Fig. 5, where (a) shows lidar data advancing towards the rotor with the cuboid centered around X_{target}, representing the spatial filtering region, and (b) maps selected measurements inside the cuboid onto the fixed YZ grid.

If multiple measurements fall into the same grid cell, only the one closest to X_{target} is retained. Panel (c) shows the resulting fluctuations after subtracting the known shear profile ($\bar{U}(y,z)$) from the LES dataset set A (refer to Sect. 2.2).

All data used in this study is gather in an publicly available dataset (Soto Sagredo et al., 2025a).

2.7 Wind-inflow reconstruction techniques

This section presents the methodologies used to reconstruct the longitudinal wind component (u) from synthetic lidar measurements obtained from the hub-lidar database (Sect. 2.6). Reconstructions are performed on a fixed 39×91 grid ($y \times z$), consistent with the global POD modes (Sect. 2.2). A total of 1200 time steps (600 s) are reconstructed with a sampling interval of $d_t = 0.5$ s.

All four methods use lidar-derived wind speed fluctuations as input, defined as $u'_{\text{lidar}}(t,y,z) = u_{\text{lidar}}(t,y,z) - \bar{U}(y,z)$, where $\bar{U}(y,z)$ is the known mean vertical wind speed profile (i.e., shear) from LES set A. This step standardizes the input across methods. After reconstructing the fluctuating component, the known shear is added back to obtain the full wind field for evaluation.

The four reconstruction techniques evaluated in this study are described below.

2.7.1 Baseline

The baseline methodology replicates the standard approach of estimating REWS from lidar measurements in LAC applications (Held and Mann, 2019). To ensure fair comparison, we account for the known shear profile. The reconstructed longitudinal wind speed at each time step is defined as:

$$u(t,y,z) = \frac{1}{n_{\text{meas}}} \sum_{i=1}^{n_{\text{meas}}} u'_{\text{lidar, i}} + \bar{U}(y,z), \tag{8}$$

where $u'_{\text{lidar},i}$ are the LOS-projected wind speed fluctuations (Sect. 2.4) within the circular region A_R defined by $[y_j^2 + (z_j - Z_{\text{hub}})^2]^{1/2} \leq 95$ m, centered at hub height in the fixed YZ grid plane (Fig. 5c). This area spans the rotor disk of the DTU 10 MW turbine with a 6 m margin to account for tower and shaft motion. The term n_{meas} denotes the number of lidar measurements available within the circular area A_R in the fixed plane.

2.7.2 Least-squares fit of POD modes

The Moore–Penrose pseudo-inverse is used to solve a least-squares problem for estimating the modal time series from lidar measurements, originally introduced by Moore (1920) and independently by Penrose (1955).

Using the projected LOS fluctuations, u'_{lidar}, this field is stored in a matrix $\mathbf{M}_{\text{lidar}} \in \mathbb{R}^{\mathrm{N}_y \times \mathrm{N}_z}$ on a regular YZ grid (Fig. 5c), with missing data points assigned `NaN` for numerical computational purposes, where $N_y = 39$ and $N_z = 91$ are the grid points across the lateral and vertical directions respectively. We define the index set $\mathcal{I} = \{i_1, i_2, \ldots, i_{n_{\text{meas}}}\}$ for grid locations with valid measurements, where n_{meas} is the number of available measurements. Hence, the measurement vector $\mathbf{D}_{\text{lidar}}$ is defined as $\mathbf{D}_{\text{lidar}} = \text{vec}(\mathbf{M}_{\text{lidar}})_{\mathcal{I}} \in \mathbb{R}^{n_{\text{lidar}}}$, where vec$(\cdot)$ denotes column-wise vectorization.

The global POD modes $\mathbf{G}$ are sub-sampled at $\mathcal{I}$ locations, and the first K global POD modes are selected to form the matrix $\mathbf{A} = \mathbf{G}_{\mathcal{I},1:K} \in \mathbb{R}^{n_{\text{meas}} \times K}$.

The modal coefficients $\tilde{\boldsymbol{\phi}}$ are computed by solving the least-squares problem via pseudo-inverse of $\mathbf{A}$, by projecting $\boldsymbol{D}_{\text{lidar}}$ onto the column space of $\mathbf{A}$, leading to $\tilde{\boldsymbol{\phi}} = (\mathbf{A}^\top \mathbf{A})^{-1} \mathbf{A}^\top \mathbf{D}_{\text{lidar}}$. The reconstructed wind field at each time step is then computed as:

$$u(t, y, z) = \sum_{i=1}^{K} g_i(y, z) \tilde{\phi}_i(t) + \bar{U}(y, z), \tag{9}$$

where $g_i(y, z)$ is the i-th POD mode and $\tilde{\phi}_i(t)$ the corresponding estimated modal amplitude. Finally, the known mean profile $\bar{U}(y, z)$ is added back to recover the full field.

2.7.3 Interpolation with IDW

IDW estimates the wind fluctuations at a target location as a weighted average of nearby measurements, where influence decreases with distance. If the target coincides with a measurement location, the interpolated value matches the measurement. Mathematically, the interpolated longitudinal velocity at position $\mathbf{x} = (t, y, z)$ is calculated as:

$$u(t, y, z) = \frac{\sum_{i=1}^{n_{meas}} w_i(\mathbf{x}) u_i'}{\sum_{i=1}^{n_{meas}} w_i(\mathbf{x})} + \bar{U}(y, z), \tag{10}$$

where u_i' is the wind speed fluctuation at measurement location $\mathbf{x_i}$, and the weights $w_i(\mathbf{x})$ are defined as:

$$w_i(\mathbf{x}) = \frac{1}{d(\mathbf{x}, \mathbf{x_i})^p}, \tag{11}$$

with $d(\mathbf{x}, \mathbf{x_i})$ the Euclidean distance between the location of unknown u' and lidar measurements u_i', and p is a positive exponent controlling the decay rate, where higher values of p emphasize nearer points. An exponent of $p = 3$ was found to minimize reconstruction errors.

2.7.4 Hybrid methodology: IDW combined with POD-LSQ

The final method combining IDW and POD-LSQ is presented in this section, called POD-IDW. First, the wind field fluctuations across the YZ plane are estimated at each time step using IDW technique, following Sect. 2.7.3. Using the resulting IDW-reconstructed fluctuations (without the added vertical shear profile), the modal amplitudes $\tilde{\boldsymbol{\phi}}$ are then estimated by performing a least-squares fit onto the global POD modes (Sect. 2.7.2).

Therefore, the modal coefficients $\tilde{\boldsymbol{\phi}}$ are computed as $\tilde{\boldsymbol{\phi}} = (\mathbf{A}^\top \mathbf{A})^{-1} \mathbf{A}^\top \boldsymbol{D}_{\text{IDW}}$, where $\boldsymbol{D}_{\text{IDW}} \in \mathbb{R}^{\text{N}_y \times \text{N}_z}$ is now the vectorization of the IDW reconstructed plane.

This hybrid approach is proposed to address a challenge encountered when using POD-LSQ: In areas without measurements, localized overfitting occurs. By using the IDW interpolated field to estimate the modal amplitudes, this limitation is mitigated.

2.8 Metrics for optimal parameter selection

Several parameters influence the accuracy of wind field reconstruction. To quantify the performance of the methods described in Sect. 2.7, we use the mean absolute error (MAE) computed within an area around the rotor, denoted as A_R (see Sect. 2.7.1). The MAE is computed over the 10-minute simulations period ($N_t = 1200$, $d_t = 0.5$ s) as:

$$MAE_{\mathrm{rotor},i,m}(\theta, n_{\mathrm{scan}}, K) = \frac{1}{\mathrm{N}_t} \sum_{t=1}^{\mathrm{N}_t} \left[\frac{1}{N} \sum_{(y,z)\in A_R} |u_{\mathrm{ref},i}(t,y,z) - u_{i,m}(t,y,z)| \right], \tag{12}$$

where N is the number of spatial grid points within the rotor area A_R, and $u_{\mathrm{ref},i}$ denotes the reference wind field for inflow case i. The index $i \in \{1, \ldots, N_{\mathrm{cases}}\}$ spans the set of inflow cases, with $N_{\mathrm{cases}} = 64$, representing 16 independent 10-minute realizations across four wind speeds $\bar{U}_o \in \{8.0, 12.0, 15.0, 20.0\}$ m s^{-1}. The subscript m represents each reconstruction method described in Sect. 2.7, with $m \in \{\text{Baseline, POD-LSQ, IDW and POD-IDW}\}$.

To enable fair comparison across different wind speeds, all reconstruction errors are normalized by the corresponding inflow mean wind speed $\bar{U}_{o,i}$. The global performance metric for a given method m is defined as:

$$MAE_{\mathrm{global},m}(\theta, n_{\mathrm{scan}}, K) = \frac{1}{\mathrm{N}_{\mathrm{cases}}} \sum_{i=1}^{\mathrm{N}_{\mathrm{cases}}} \left(\frac{MAE_{\mathrm{rotor},i,m}(\theta, n_{\mathrm{scan}}, K)}{\bar{U}_{o,i}} \right). \tag{13}$$

The global reconstruction performance depends on several key parameters. First, the half-cone opening angle θ directly influences the spatial distribution and availability of lidar measurements across the rotor, as well as potential cross-contamination effects. In this study, we evaluate θ values in the range $\theta \in \{10.0°, 12.5°, \ldots, 50.0°\}$, using the same angle for all six beams.

Second, the number of lidar measurements per time step, n_{meas}, depends on the selected number of lidar scans, $n_{\mathrm{scan}} \in \{1, 2, \ldots, 8\}$ (see Sect. 2.6). Increasing n_{scan} provides higher data availability, but it can degrade reconstruction due to higher spatial filtering.

For POD-based methods, the number of retained modes K is another important parameter. A higher K allows for finer-scale flow reconstruction but can increase sensitivity to measurement sparsity and lead to overfitting. We evaluate $K \in \{10, 20, 30, 40, 50, 75, 100, 125, 150, 200\}$.

The optimal parameter combination for each method, $(\theta_{\mathrm{opt},m}, n_{\mathrm{scan,opt},m}, K_{\mathrm{opt},m})$, is defined as the one that minimizes the global normalized reconstruction error:

$$(\theta_{\mathrm{opt},m}, n_{\mathrm{scan,opt},m}, K_{\mathrm{opt},m}) = \arg \min_{\theta, n_{\mathrm{scan}}, K} \{MAE_{\mathrm{global},m}(\theta, n_{\mathrm{scan}}, K)\}, \tag{14}$$

where the search spans all 1,360 ($17 \times 8 \times 10$) combinations in the discrete parameter space.

3 Results

To evaluate the performance and characteristics of the proposed reconstruction methods, we begin by assessing the accuracy of the modal amplitude estimation for POD-LSQ using lidar measurements, as discussed in Sect. 3.1. We then examine how

the number of scans and modes influences the spectral content of the reconstructed inflow fields in Sect. 3.2. The effect of the half-cone opening angle on reconstruction accuracy is analyzed in Sect. 3.3, while Sect. 3.4 investigates the influence of wind speed quantity. Finally, Sect. 3.5 synthesizes these findings and presents a discussion on the optimal parameter configuration for each method.

To assess the influence of wind speed quantity selection has in reconstruction accuracy, we compare the reconstruction results using three wind speed quantities, hereafter referred to as: (i) the volume-averaged lidar estimate, $u_{\text{lidar, wgh}}$, representing LOS velocities projected into the longitudinal direction and averaged over the lidar probe volume; (ii) the nominal lidar estimate, $u_{\text{lidar, nom}}$, obtained from the same projection procedure but without applying volume averaging; and (iii) the true wind speed, u_{fw}, corresponding to the reference longitudinal wind velocity extracted from the reference LES inflow field at the same grid locations in the X_{target} plane where the lidar measurements are fixed (see Fig. 5c) at each time step.

While only $u_{\text{lidar, wgh}}$ represents a physically realistic lidar input, the alternative wind speed definitions are used for diagnostic purposes. In particular, u_{fw} isolates the performance of the reconstruction methods from key sources of measurement uncertainty, including volume averaging, cross-contamination, tower motion, and multi-distance fixed-plane mapping error. The latter refers to the spatial inconsistency introduced when lidar measurements—collected at different longitudinal positions—are projected onto a fixed estimation plane (X_{target}), ignoring their true spatial separation along the longitudinal direction. In contrast, the difference between $u_{\text{lidar, nom}}$ and $u_{\text{lidar, wgh}}$ isolates the effect of volume averaging alone. These three wind speed definitions are used consistently throughout the paper to evaluate reconstruction accuracy and quantify the impact of measurement-related uncertainties.

3.1 Modal amplitude estimation with POD-LSQ

In real-time applications, reconstructing wind fields at each time step using global POD modes requires estimating the corresponding modal amplitudes, $\tilde{\phi}(t)$. This estimation is carried out using the POD-LSQ approach described in Sect. 2.7.2. In this section, we evaluate how wind speed quantity selection affects the accuracy of these modal amplitude estimations.

Figure 6 presents the first five modal amplitudes for a representative 10-minute inflow case with a mean wind speed of $\bar{U}_o = 15.35$ m s^{-1}. The reference modal amplitudes (solid black lines) are compared against those estimated by POD-LSQ (dashed orange lines), using $K = 50$ global POD modes, $n_{\text{scan}} = 7$ scans, and a half-cone angle of $\theta = 22.5°$. The top row of Fig. 6 shows results obtained using the true wind speed as input, second row uses the nominal lidar estimate (without volume-averaged), while the bottom row uses the volume-averaged lidar estimate. This comparison allows us to isolate and quantify the impact of measurement errors on the estimation of modal amplitudes. Each subplot also reports the normalized MAE, defined as MAE/σ, where σ is the standard deviation of the corresponding reference amplitude.

As expected, the estimation error MAE/σ increases with mode number. Lower-order modes (e.g., Modes 1–3), which represent dominant large-scale structures, are reconstructed more accurately than higher-order modes (e.g., Modes 4–5), which correspond to finer-scale features. Furthermore, the use of the lidar-based estimates leads to consistently higher reconstruction errors compared to using the true wind speed. For mode 1, MAE/σ increases by 55% when using nominal lidar estimate compared to the true wind speed, while an increase of 41% is observed for volume-averaged lidar estimate. For mode 5, these

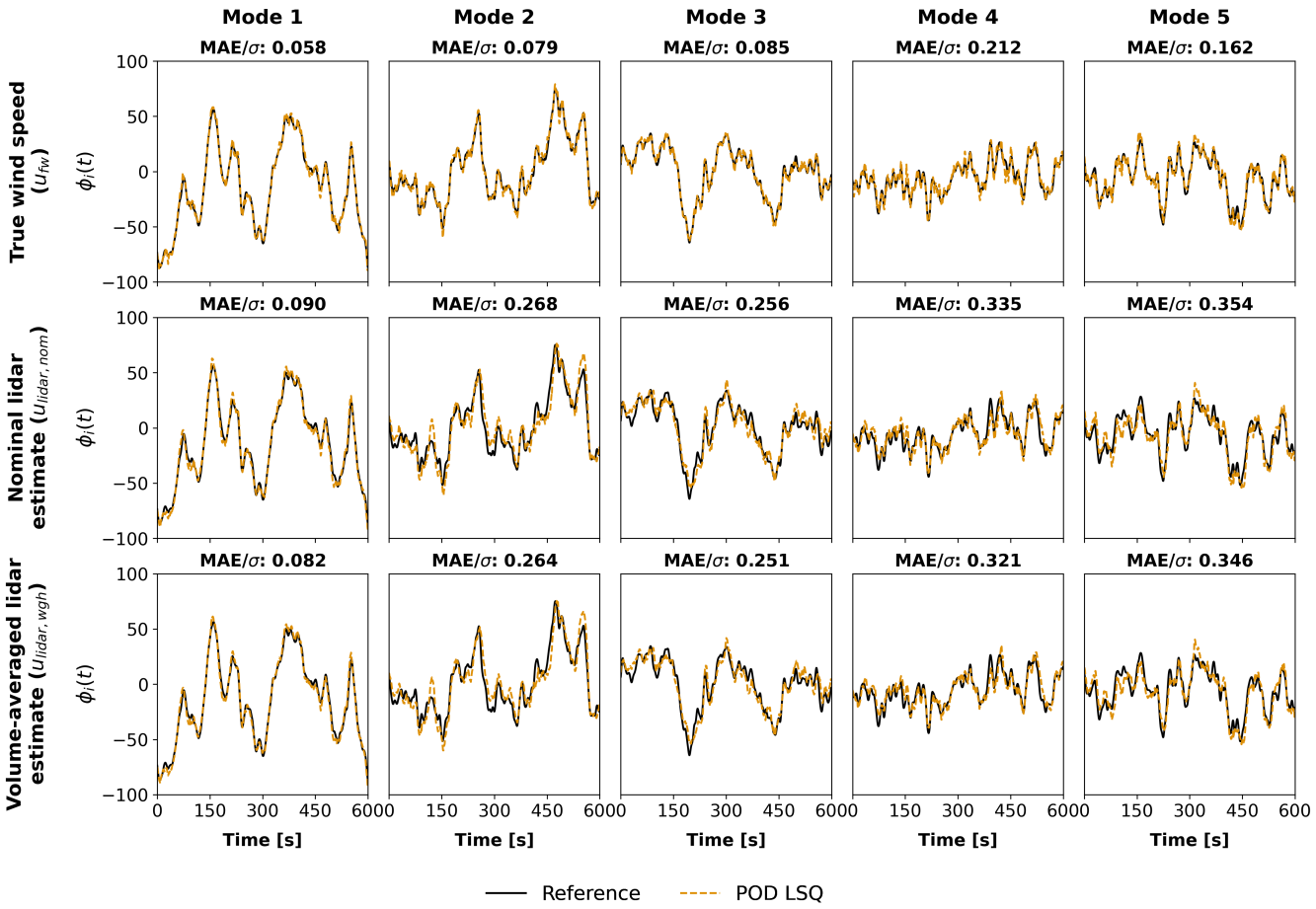

Figure 6. First five modal amplitudes estimated using POD-LSQ with $K = 50$ global POD modes, $n_{\text{scan}} = 7$ scans, and half-cone angle $\theta = 22.5^{\circ}$. Top row: estimation using true wind speed (u_{fw}); second row: estimation using nominal lidar estimated ($u_{\text{lidar, nom}}$) wind speed; bottom row: estimation using volume-averaged lidar estimated ($u_{\text{lidar, wgh}}$) wind speed.

differences become more pronounced, with increases of 119% and 114%, respectively. These results highlight the sensitivity of modal amplitude estimation to measurement-related uncertainties—such as cross-contamination, spatial offsets resulting from the fixed-grid filtering approach used for multi-distance lidar measurements, and tower-induced motion. Higher-order modes are particularly affected by these effects. Notably, probe volume-averaged helps to reduce such errors, as reflected in the consistently lower MAE/σ values compared to the nominal case.

3.2 Sensitivity to number of scans and modes on the spectral content

To assess how the number of scans and modes affects the reconstruction of turbulent inflow fields, we analyze the power spectral density (PSD) of the u-velocity fluctuations for a representative case with $\bar{U}_o = 15.35$ m s^{-1} over a 10-minute simulation. The

PSD is estimated using Welch's method with a Hamming window, six segments, and 50% overlap. To characterize the spectral energy content across the full rotor plane rather than just the rotor-averaged wind speed, the PSD is computed point-wise and subsequently averaged over all grid points within the area A_R (refer to Sect. 2.7.1):

$$\mathrm{PSD}_{\mathrm{avg}}(f) = \frac{1}{N_{\mathrm{grid}}} \sum_{i=1}^{N_{\mathrm{grid}}} S_{ii}(f), \tag{15}$$

where $S_{ii}(f)$ is the power spectrum estimated at grid point $i \in A_R$ and N_{grid} is the total number of grid points inside A_R.

3.2.1 Number of scans and estimation method

This section compares the PSD of the original flow to the estimated flow for different estimation methods and numbers of scans. The number of modes used in the POD-based estimation methods is kept fixed for this analysis; the impact of POD modes is analyzed in detail in Sect. 3.2.2.

Figure 7 presents the PSD results for (a) Baseline, (b) POD-LSQ, (c) IDW, and (d) POD-IDW, using $\theta = 22.5°$ and $K = 100$ global POD modes. Each panel shows reconstructions for various numbers of lidar scans ($n_{\mathrm{scan}} \in \{4, 8, 12, 16\}$) and two types of wind speed inputs: the true wind speed (u_{fw}, solid lines) and the volume-averaged lidar estimate ($u_{\mathrm{lidar,\ wgh}}$, dashed lines). For reference, the full LES turbulence spectrum is plotted in solid black. The truncated POD spectrum (gray dashed) corresponds to the projection of the LES flow onto the first 100 POD modes using the standard inner product, which is a better basis of comparison for the POD methods. The vertical dashed line indicates the tower's first fore-aft eigenfrequency, f_{tower}. The energy drop-off beyond 0.1 Hz in the LES reference is attributed to grid resolution limitations, as reported in Thedin et al. (2023); Doubrawa et al. (2019); Rivera-Arreba et al. (2022). Similarly, the further roll-off observed in the truncated POD spectrum is due to modal truncation. As noted by Liverud Krathe et al. (2025), these high-frequency limitations do not significantly affect fatigue analysis outcomes.

Low frequencies

At frequencies below 0.1 Hz, all reconstruction methods except the baseline (Fig. 7a) closely follow the LES spectrum when estimating using the true wind speed u_{fw} (solid lines). The baseline method is formulated as a rotor-equivalent estimate combined with the prescribed mean shear profile, such that the time-varying component is spatially uniform across the rotor plane. Consequently, it does not reproduce spatially varying turbulent fluctuations at individual grid points within A_R. Because the spectra are obtained by averaging point-wise PSDs over all grid points inside A_R, the baseline's rotor-averaging inherently reduces energy in the spatially resolved u spectra, including at low frequencies.

IDW effectively reproduces the LES spectrum, while POD-based methods align with the truncated POD reference, consistent with their basis truncation. In contrast, reconstructions based on the volume-averaged lidar estimate consistently exhibit lower energy from 0.02 Hz upwards. This reduced energy results from two sources of spatial filtering: the intrinsic averaging within the probe volume (Peña et al., 2017) and the measurement selection procedure, which maps multi-distance observations—taken at varying longitudinal positions—onto a fixed grid. This process smooths out turbulent fluctuations by blending information across different regions of the inflow. This filtering effect also impacts the baseline method, though to a lesser extent given its already simplified reconstruction approach.

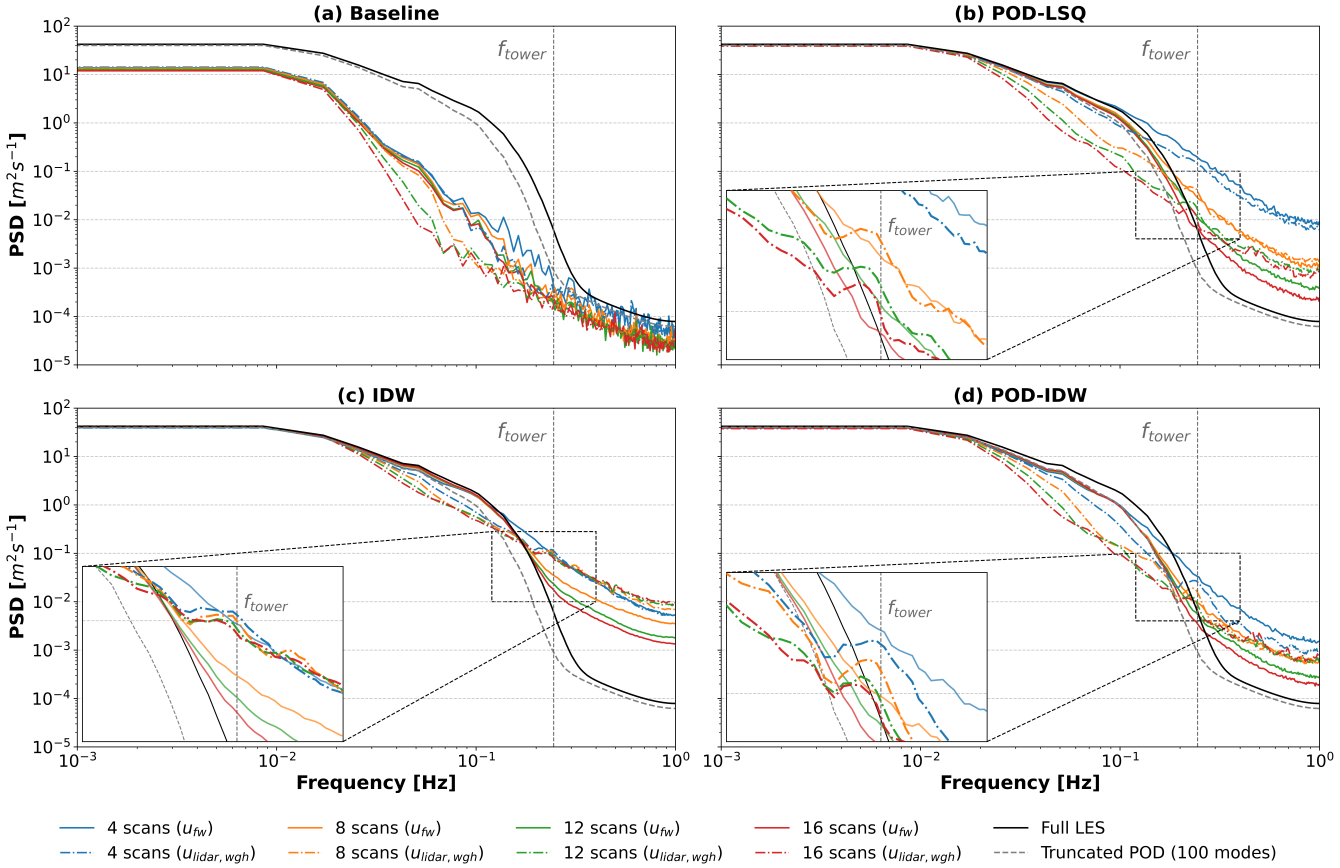

Figure 7. Influence of the number of scans n_{scan} on the turbulence spectra of the u-component over a 10-minute simulation for each method, using $\theta = 22.5°$, $K = 100$ global POD modes for POD-based methods, for the true wind speed (u_{fw}) and volume-averaged lidar estimate ($u_{\text{lidar, wgh}}$) as input parameters for the reconstruction. Welch's method with Hamming window (six segments, 50% overlap) is applied and the PSDs around the area A_R (see Sect. 2.7.1) around the rotor area averaged for smoothing.

High frequencies

In the high-frequency range, the flow estimated using POD-LSQ, POD-IDW, and IDW has more energy than the LES flow for both u_{fw} and volume-averaged lidar estimate. When using u_{fw}, increasing the scan count reduces this extra spectral energy for these methods, drawing their spectra closer to the LES reference. This reduction in high-energy content with higher scans is driven by the number of available measurements in the rotor plane, which increases with n_{scan}. For example, in this study, four scans correspond to approximately 15% coverage of the YZ plane, while 16 scans increases that coverage to around 42%. Having more measurements in the rotor plane reduces overfitting for the POD methods, which results in lower spectral energy for more scans. In IDW, a higher number of measurements increases spatial coverage, reducing gaps between data points. This leads to more accurate interpolation and lower reconstruction error.

However, for lidar-based inputs, the measurement selection procedure described in Sect.2.6 selects data points across varying longitudinal positions and maps them onto a fixed grid, which becomes increasingly extended as more scans are included. This introduces an additional spatial filtering effect, resulting in a sharper energy drop beyond 0.017 Hz. While IDW does not exhibit the same steep decline, this instead reflects increased noise due to higher multi-distance fixed-plane mapping errors, rather than improved reconstruction fidelity. Unlike POD-based methods, which enforce spatial coherence through a global modal basis, IDW does not incorporate spatial correlations between measurements, which can compromise accuracy, especially for irregularly distributed data (Li et al., 2020; Bokati et al., 2022). Furthermore, IDW assumes isotropic flow variations and is sensitive to outliers, making it more susceptible to errors caused by spatial separation. This behavior is further illustrated in the time series example for $n_{\text{scan}} = 16$ shown in Appendix C.

Tower natural frequency

A secondary effect visible in Fig. 7 is the presence of a peak near the tower's natural frequency, $f_{\text{tower}} = 0.25$ Hz, in the volume-averaged lidar estimate reconstructions (zoomed area). This is caused by tower-induced motion distorting the lidar measurements. The effect is particularly visible when $n_{\text{scan}} = 4k$ for $k \in \mathbb{N}$, since four scans approximately matches the tower's oscillation period. The peak is more pronounced in POD-based reconstructions and less distinguishable in IDW due to IDW's elevated background spectral energy near f_{tower}.

3.2.2 Number of POD modes

This section demonstrates the impact of number of POD modes on the estimation for the POD-LSQ and POD-IDW methods, where n_{scan} is kept constant.

Figure 8 presents the PSD for (a) POD-LSQ and (b) POD-IDW for different numbers of modes, $K \in \{50, 100, 150, 200\}$, using $n_{\text{scan}} = 4$, $\theta = 22.5°$, and the volume-averaged lidar estimate as input. Lower values of K capture the large-scale, low-frequency content of the flow, while increasing K introduces more high-frequency energy. At low frequencies, POD-LSQ aligns more closely with the truncated POD spectrum, whereas POD-IDW shows greater deviation due to the influence of the initial IDW plane, which introduces interpolation-related errors. At higher frequencies (above 0.1 Hz), POD-LSQ tends to overestimate energy, primarily due to overfitting in the modal amplitude estimation, as mentioned in Sect 3.2.1. This effect will be discussed again in Sect. 3.3. POD-IDW mitigates overfitting by using the IDW-reconstructed plane as input for estimating modal amplitudes, which smooths the high-frequency content and reduces overfitting.

3.2.3 Summary and methodological implications

The scan count, n_{scan}, exerts a dual influence on reconstruction quality. On the one hand, increasing n_{scan} improves fidelity when using ideal inputs (u_{fw}) by enhancing spatial coverage. On the other hand, it also increases the longitudinal separation between measurements, which can degrade reconstruction accuracy when lidar-based inputs ($u_{\text{lidar, wgh}}$) are used due to amplified multi-distance fixed-plane mapping error.

Each reconstruction method responds differently to this trade-off. IDW is particularly sensitive to spatial separation, as it does not account for spatial correlation across measurements. POD-LSQ, by contrast, is more affected by the number and

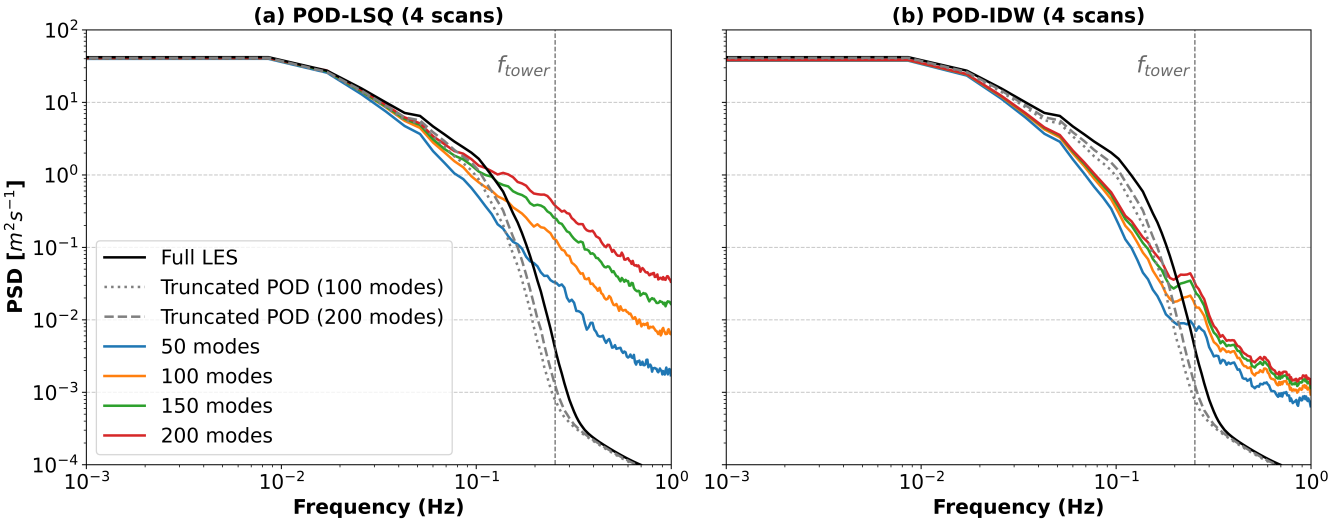

Figure 8. Influence of the number of POD modes (K) on the turbulence spectra of the u-component over a 10-minute simulation for POD-LSQ (a) and POD-IDW (b), with $K \in 50, 100, 150, 200$ and $n_{\text{scan}} = 4$. Welch's method is applied (six segments, 50% overlap) over the interest area A_R (see Sect. 2.7.1).

distribution of available measurements—especially at higher values of K—since accurate estimation of modal amplitudes requires adequate spatial coverage. POD-IDW, which combines an initial IDW interpolation with subsequent POD fitting, inherits some limitations from the interpolation step but benefits from the modal projection, which helps to smooth errors introduced by spatial filtering (refer to Appendix C). As a result, the optimal selection of both scan count (n_{scan}) and number of POD modes (K) should be tailored to the specific sensitivities of each method and the nature of the available input.

Finally, attention should be given to the effects of tower motion, which introduce spurious energy near the tower's natural frequency (f_{tower}). These artifacts, particularly prominent in lidar-based reconstructions, require correction techniques or frequency-domain filtering to avoid negative impacts on both control performance and aeroelastic load assessments.

3.3 Effect of half-cone angle on reconstruction performance

The selection of the half-cone angle, θ, affects reconstruction accuracy in two main ways: (1) by influencing the number and spatial distribution of lidar measurements across the rotor plane, and (2) by increasing cross-contamination in the volume-averaged lidar estimate derived from LOS measurements.

Figure 9 illustrates these effects at a representative time step across the YZ rotor plane. Each column corresponds to a half-cone angle $\theta \in \{10.0°, 17.5°, 20.0°, 22.5°, 35.0°, 50.0°\}$ using $K = 200$ modes and $n_{\text{scan}} = 4$ for all reconstructions. Row (a) shows the location of the lidar measurements, and each point's color represents the difference between the true wind speed (u_{fw}) and the volume-averaged lidar estimate ($u_{\text{lidar, wgh}}$), while rows (b)–(e) present reconstruction errors relative to the LES reference for (b) Baseline, (c) POD-LSQ, (d) IDW, and (e) POD-IDW. MAE values are reported above each case.

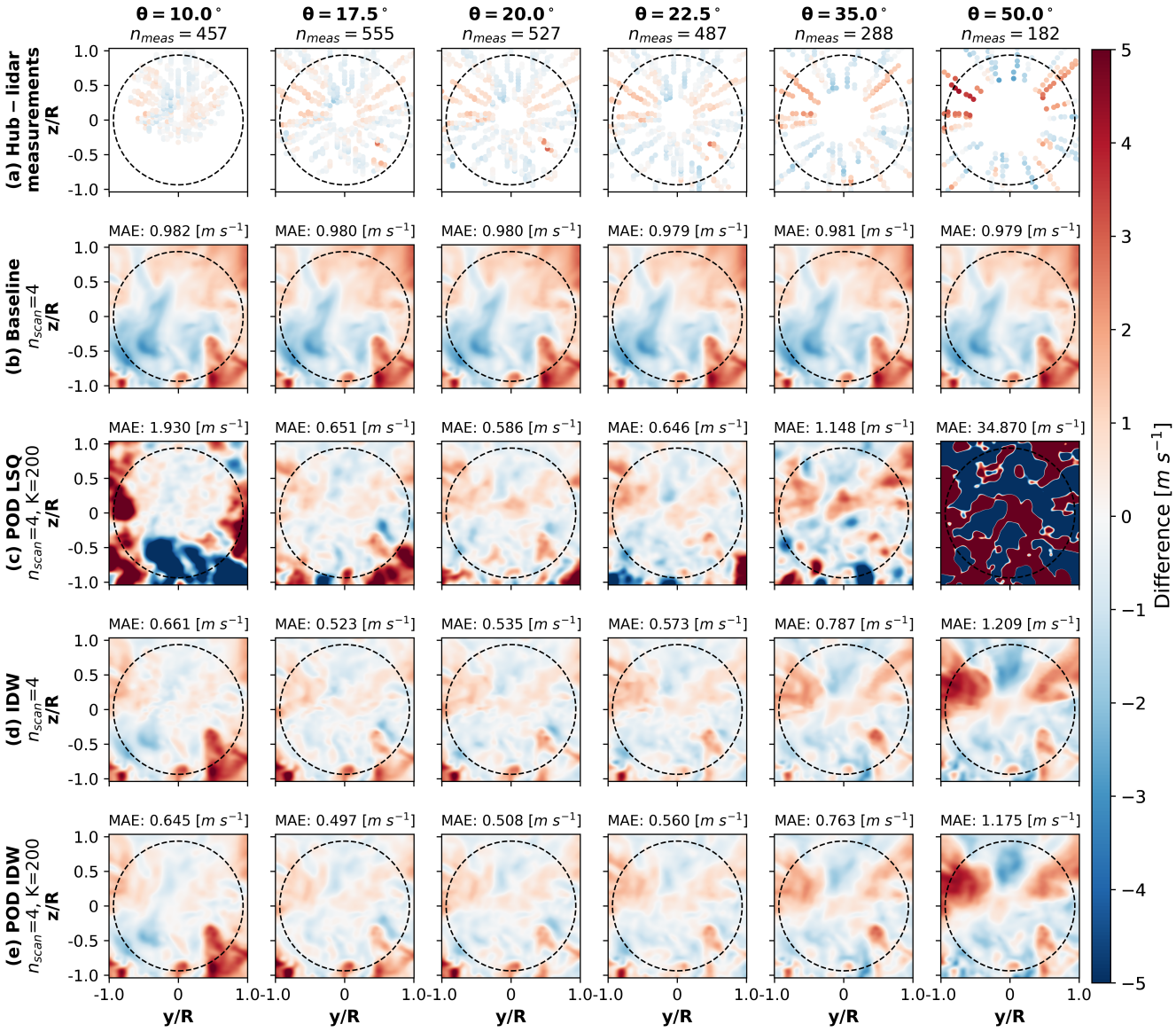

Figure 9. Difference across the YZ plane between the reconstructed ($u(t, y, z)$) and reference ($u_{\text{ref}}(t, y, z)$) wind fields, for $\bar{U}_o = 15.35$ m s^{-1} at a single time step. The columns correspond to increasing half-cone angles from 10° to 50°, using four scans and 200 POD modes, where (a) shows the difference between the hub-lidar volume average projected LOS measurements ($u_{\text{lidar, wgh}}$) and the true wind speed (u_{fw}), and (b)–(e) present the differences between the reconstructed and LES reference cases for (b) baseline, (c) POD-LSQ, (d) IDW, and (e) POD-IDW. Blue colors indicate underestimation, while red colors indicate overestimation of wind speeds relative to the reference field. The black dashed circle indicates the DTU 10 MW RWT rotor ($R = 89$ m).

As shown in Fig. 9a, at $\theta = 10.0°$, measurements concentrate near the upper center of the rotor due to turbine tilt, yielding $n_{\text{meas}} = 457$. With increasing θ, spatial coverage improves as measurements spread more broadly across the rotor plane. However, beyond a certain point, outer beams extend beyond the rotor, reducing central coverage. For example, at $\theta = 50.0°$, only 182 valid measurements remain as outer range gates extend beyond the rotor area due to beam inclination. Additionally, larger θ values increase cross-contamination—indicated by the more intense coloring of the points—due to increased misalignment with the line-of-sight and the longitudinal turbulence.

Figure 9b–e shows how each method responds to changes in θ. The baseline method is relatively insensitive, exhibiting consistent performance across all angles. POD-LSQ, in contrast, is highly sensitive, as accuracy depends on both the number and spatial distribution of measurements. At $\theta = 10.0°$, performance degrades despite a high measurement count due to poor spatial coverage and localized overfitting. At $\theta = 50.0°$, the number of measurements is too low ($n_{\text{meas}} = 182$) to support fitting $K = 200$ modes, yielding an underdetermined system and degraded accuracy. These results highlight that, for POD-based methods, ensuring $n_{\text{meas}} \geq K$ is necessary but not sufficient—broad spatial coverage is equally critical. Notably, although $\theta = 10.0°$ yields more measurements than $\theta = 35.0°$, POD-LSQ performs worse, underscoring the importance of spatial distribution over raw measurement count.

The sensitivity of IDW and POD-IDW to θ is less significant than for POD-LSQ. However, both methods exhibit increased reconstruction error at $\theta = 50.0°$, consistent with greater cross-contamination in the LOS-derived wind speed (Fig. 9a). POD-IDW inherits interpolation errors from the IDW field, so spatial inaccuracies propagate into the final reconstruction. Still, applying POD over the IDW field reduces spatial inconsistencies, resulting in smoother fields and improved performance over IDW alone—though the improvement in MAE is limited (Fig. 9d-e).

Careful selection of the half-cone angle is therefore essential, particularly for POD-based methods. The angle must balance spatial coverage with minimal contamination from v and w components in the LOS signal. This selection depends on lidar geometry, turbine tilt, and alignment between beam orientation and the rotor plane. It is also critical to ensure that $n_{\text{meas}} \geq K$, and that measurements are sufficiently distributed to avoid overfitting in POD-LSQ. The baseline method, by contrast, remains largely insensitive to θ, provided enough data are collected across the scan radius (Simley et al., 2018).

3.4 Impact of wind speed quantity on reconstruction performance

To assess how lidar-induced measurement errors affects reconstruction accuracy, we evaluate each method using the three wind speed inputs: (i) true wind speed (u_{fw}), (ii) nominal lidar estimate without volume averaging ($u_{\text{lidar, nom}}$), and (iii) volume-averaged lidar estimate ($u_{\text{lidar, wgh}}$).

Figure 10 shows the global reconstruction error, MAE_{global} (defined in Sect. 2.8), as a function of the half-cone angle θ for each method using its optimal configuration, $n_{\text{scan,opt}}$ and K_{opt}, determined as shown in Fig. 2 and listed in Table 1. Results are presented for four methods—(a) Baseline, (b) POD-LSQ, (c) IDW, and (d) POD-IDW—under all three wind speed inputs. The performance spread across these inputs reflects the influence of measurement errors and volume averaging. A more comprehensive sensitivity analysis over θ, n_{scan}, and (where applicable) K, including the full set of heat maps used to identify the method-specific optima, is provided in Appendix D.

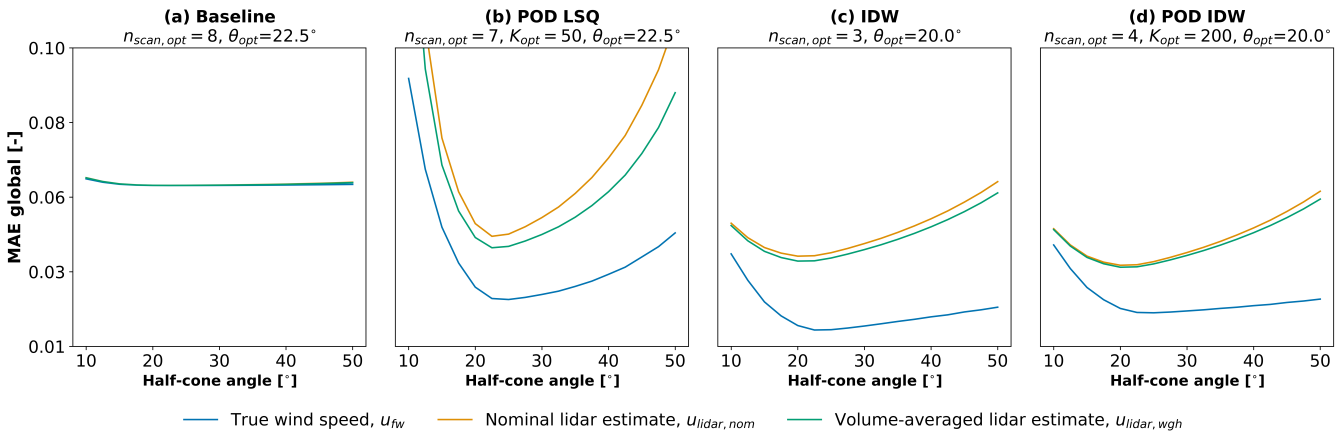

Figure 10. Global mean absolute error, MAE_{global}, as a function of half-cone angle, θ, for the best-performing configurations: (a) baseline, (b) POD-LSQ, (c) IDW, and (d) POD-IDW. Results are shown using: true wind speed (u_{fw}, blue), nominal estimate ($u_{\text{lidar, nom}}$, orange), and volume-averaged estimate ($u_{\text{lidar, wgh}}$, green).

Consistent with Sect. 3.3, the baseline method (Fig. 10a) shows almost identical results regardless of input type, due to its rotor-averaging approach that inherently smooths spatial uncertainties. Overall, the baseline yields larger reconstruction errors than the spatial reconstruction methods across most of the parameter space; however, for extreme half-cone angles, POD–LSQ can perform worse than the baseline. Among the other methods, POD-LSQ remains the most sensitive to half-cone angle selection, with errors increasing sharply as θ deviates from the optimum due to overfitting and cross-contamination, which impair modal amplitude estimation (see also Sects. 3.2 and 3.3). In contrast, IDW and POD-IDW show less sensitivity to θ, with errors remaining relatively stable even as measurement distribution deteriorates. For POD-IDW, this robustness is partly inherited from IDW, as it uses the interpolated IDW field for modal fitting and thus avoids overfitting (see Sect. 3.3).

IDW shows the largest performance gap between u_{fw} and lidar-based inputs, highlighting its strong sensitivity to uncertainties, particularly the multi-distance fixed-plane mapping error and cross-contamination. POD-IDW performs slightly better, as the modal decomposition enforces spatial coherence, mitigating some interpolation-related errors. POD-LSQ also benefits from modal constraints, reducing sensitivity to input uncertainty, though it remains highly dependent on θ.

Across all methods, reconstructions using the true wind speed u_{fw} significantly outperform those from the two line-of-sight quantities, but the volume-averaged input ($u_{\text{lidar, wgh}}$) outperforms the nominal lidar estimates ($u_{\text{lidar, nom}}$). In other words, there is a significant increase in error caused by measurement inaccuracies, but adding volume averaging actually reduces the error. This demonstrates the benefit of modeling the probe volume, as volume averaging reduces cross-contamination and improves reconstruction quality—a trend especially evident for POD-LSQ and consistent with the findings reported in Soto Sagredo et al. (2025b).

In summary, reconstruction accuracy is significantly influenced by measurement quantity. IDW is the most affected, followed by POD-IDW, which inherits interpolation errors. POD-LSQ shows better resilience but depends strongly on appropriate

angle selection. The baseline, though robust to measurement variations, performs worst overall. These results emphasize the importance of ~~accounting for probe volume effects and~~ tuning method-specific parameters for reliable lidar-based wind field reconstruction.

3.5 Overall method performance

The ultimate conclusion we would like to draw is which of the investigated methods performs "best." The optimal parameter sets—half-cone angle θ_{opt}, number of scans $n_{\text{scan,opt}}$, and number of POD modes K_{opt}—are those that minimize the global mean absolute error MAE_{global} for each reconstruction method (Sect. 2.8). These values are summarized in Table 1 for both the true wind speed input (u_{fw}) and the volume-averaged lidar estimate ($u_{\text{lidar, wgh}}$), with corresponding performance trends shown in Fig. 10.

Table 1. Optimal parameter combinations $(\theta_{\text{opt}}, n_{\text{scan,opt}}, K_{\text{opt}})$ that minimize the global mean absolute error, MAE_{global}, for each reconstruction method, using as inputs the true wind speed (u_{fw}) and volume-averaged lidar estimated wind speed ($u_{\text{lidar, wgh}}$).

Method	Wind speed input	θ_{opt}	$n_{\text{scan, opt}}$	$\bar{n}_{\text{meas}}$	K_{opt}	MAE_{global}	Error compared to baseline
Baseline	True wind	22.5°	8	868	-	0.0549	-0.04 %
	Volume-averaged	22.5°	8	868	-	0.0549	Reference case
POD-LSQ	True wind	25.0°	8	791	200	0.0206	-58.8 %
	Volume-averaged	22.5°	7	776	50	0.0328	-39.4 %
IDW	True wind	22.5°	8	868	-	0.0120	-74.5 %
	Volume-averaged	20.0°	3	403	-	0.0288	-44.9 %
POD-IDW	True wind	25.0°	8	791	200	0.0183	-65.6 %
	Volume-averaged	20.0°	4	518	200	0.0287	- 45.4 %

Using lidar-based input, POD-IDW achieves the lowest reconstruction error, with a 45.4% reduction in MAE_{global} compared to the baseline. IDW performs nearly as well (44.9% reduction), followed by POD-LSQ (39.4%). With true wind input, IDW achieves the best accuracy (74.5% reduction), followed by POD-IDW (65.6%) and POD-LSQ (58.8%). For the baseline, only a negligible 0.04% difference exists between input types—reflecting its robustness to uncertainty but also its limited resolution, which results in the highest reconstruction error overall. Note that the baseline method achieves its best performance with $n_{\text{scan}} = 8$, although using fewer scans results in nearly identical accuracy. This insensitivity to scan count reflects the inherent spatial averaging of the baseline approach.

Measurement errors—including probe volume averaging, cross-contamination, multi-distance fixed-plane mapping error, and tower motion—degrades reconstruction accuracy for all methods except the baseline. This effect is most pronounced for IDW (Sects. 3.2–3.4), where the error reduction drops from 74.5% (with u_{fw}) to 44.9% (with $u_{\text{lidar, wgh}}$), and the optimal number of scans decreases from eight to three. These shifts reflect IDW's strong sensitivity to the assumption that all selected

measurements lie on the same plane, neglecting their actual longitudinal location in space. For all methods, using true wind input generally shifts the optimal half-cone angle θ upward by 2.5–5°, as cross-contamination is no longer a limiting factor. POD-LSQ, in particular, improves its performance by increasing the number of modes from 50 to 200 with only one additional scan, highlighting the impact of measurement uncertainty on modal amplitude estimation (Sect. 3.1).

Overall, POD-IDW offers the best reconstruction accuracy with lidar-based inputs but comes with a higher computational cost. IDW is simpler and moderately expensive, but does not capture spatial correlations and assumes isotropic flow variations, leading to unrealistic estimates under certain conditions. POD-LSQ provides a good balance between accuracy and efficiency but requires careful tuning of lidar configuration and POD parameters. The baseline method is the fastest and most robust to measurement uncertainty, yet consistently delivers the poorest reconstruction quality. Ultimately, reliable wind field reconstruction depends on accounting for measurement uncertainty and appropriately tuning method-specific parameters.

4 Discussion

The goal of this study was to assess the reconstruction accuracy and robustness of three methods under semi-realistic inflow conditions, using LES-generated data and a hub-mounted lidar simulator. Evaluation was based on a global metric, MAE_{global}, which quantifies the deviation from the true inflow field across multiple conditions. While effective for identifying optimal parameters and quantifying deviations from the reference wind field, this metric does not capture the ability of the reconstructed fields to drive realistic turbine dynamics. A more robust analysis would involve evaluating the reconstruction error on turbine load channels, which is the subject of future work.

The current study makes several simplifying assumptions due to limitations in the available tools. Notably, the HAWC2 lidar implementation does not account for turbulence evolution (Bossanyi, 2013; de Maré and Mann, 2016) or induction effects (Borraccino et al., 2017; Mann et al., 2018), as it is based on Taylor's frozen turbulence hypothesis and BEM-based inflow dynamics. As a result, the inflow is treated as a stationary free-stream field, from where the lidar measurements are extracted. Although this is not realistic, it provides a controlled environment to evaluate reconstruction accuracy. Future work should incorporate 4D inflow fields from LES simulations that include these effects to better evaluate how they influence reconstruction performance—and how they may be compensated in practice.

All methods in this study also rely on knowledge of the mean shear profile to reconstruct the flow. This allows a consistent comparison across methods and avoids introducing additional shear estimation uncertainties. Although accurate shear estimation from hub-lidar data is feasible over longer time frames, following similar procedure to the one described in Eq.(4) from Sebastiani et al. (2022), it was not the focus of this study. Importantly, POD-based methods require subtraction of the mean flow to eliminate trends during the estimation of the modal amplitudes. In contrast, IDW and the baseline approach can operate directly on lidar measurements without prior shear estimation. Furthermore, this study focused on neutral boundary layer conditions with a turbulence intensity around 11%, which are representative but do not encompass the full range of field scenarios. Extending the evaluation to different atmospheric conditions—including stable and unstable stratification—would broaden validation.

The real-time performance of the proposed reconstruction methods was evaluated to confirm their suitability for online applications. On a standard PC using a Python implementation and input from four lidar scans (≈520 measurements), the baseline method required ≈19 ms per time step. POD-LSQ introduced minimal overhead, increasing computational time by only 7% (to ≈20 ms). In contrast, IDW was more computationally demanding, requiring 4.5× the baseline duration (≈86 ms), due to the cost of the interpolation step. POD-IDW, which combines interpolation with a subsequent POD fitting, was the most expensive at ≈103 ms per time step (5.4 × the baseline). Despite the higher cost for IDW and POD-IDW, all methods remained within practical real-time constraints.

The methods proposed in this study are not well suited for nacelle-mounted lidar systems—the most common configuration for wind turbine-mounted lidars (Letizia et al., 2023)—due to their limited spatial resolution and blade blockage, which reduce the number of available measurements. The accuracy of methods like POD-LSQ depends on having a high number of spatially distributed inputs. Moreover, the hub-lidar scanning pattern in this study was optimized for the rated rotor speed of the DTU 10 MW turbine; other turbines or operating conditions would require re-optimization to ensure adequate coverage.

Finally, real-world lidar systems also face additional uncertainties, such as optical misalignment, Doppler noise, signal processing errors, and probe volume smearing. It is also critical to ensure sufficient lead time for control while accounting for latency, memory constraints, and turbulence advection. Future work should address these challenges through adaptive filtering and selection strategies (Schlipf, 2016), validated in conjunction with flow-aware control.

5 Conclusions

This study proposed and evaluated three methodologies for real-time reconstruction of wind inflow fields across the full rotor plane, using lidar measurements extracted from LES simulations via a numerical hub-mounted lidar model in HAWC2. The methods include: POD-LSQ, which fits lidar data to a global POD basis using least squares; IDW, which interpolates the flow using inverse distance weighting from lidar data; and POD-IDW, a hybrid that estimates modal amplitudes from the IDW-reconstructed field. All were benchmarked against a baseline rotor-averaged approach based on conventional REWS estimation, a standard practice for LAC applications, that accounts for the mean known shear across the rotor plane.

When optimally configured, all proposed methods significantly outperformed the baseline, offering improved spatial resolution and turbulence reconstruction. POD-IDW achieved the lowest reconstruction error, reducing MAE_{global} by 45.4% compared to the baseline estimation, followed by IDW (44.9% reduction) and POD-LSQ (39.4% reduction). All methods met real-time computational requirements. On a standard PC with four lidar scans (≈520 measurements), the baseline required ≈19 ms per time step, while POD-LSQ added only 7% overhead. IDW and POD-IDW required ≈86 ms and ≈103 ms, respectively, but remained within practical limits.

Reconstruction performance was found to depend strongly on the number and spatial distribution of measurements, half-cone angle, measurement uncertainty, and the number of POD modes. POD-LSQ was especially sensitive to half-cone angle due to the trade-off between number of measurements in the rotor plane and measurement coverage, which can lead to overfitting with higher numbers of modes. For POD-based methods, increasing the number of global modes K increased the ability to

capture flow energy and improve inflow reconstruction, but required $K \leq n_{\text{meas}}$ and good coverage around the rotor to ensure numerical stability. POD-IDW relaxed this constraint by using a full interpolated field, supporting higher K values at the cost of propagating interpolation errors and increased computational demand.

Measurement uncertainty had a notable impact, particularly for IDW and POD-IDW, which reconstruct the full plane directly from lidar data. IDW was most affected by multi-distance fixed-plane mapping errors and performed best with fewer scans due to its lack of spatial correlation modeling. The marginal accuracy gain between POD-IDW and IDW (0.5%) reflects the trade-off between reduced overfitting and inherited interpolation error. POD-LSQ also exhibited sensitivity, as uncertainties propagated through the modal amplitude fitting process. Overall, POD-LSQ offers the best compromise between reconstruction accuracy, computational efficiency, and robustness to lidar-related uncertainties—provided that adequate spatial coverage and a sufficient number of measurements are available to support the selected number of POD modes. By projecting lidar measurements onto a set of spatial patterns derived from POD, the method captures the dominant flow structures. This enables reliable spatial reconstruction even under imperfect measurement conditions, making POD-LSQ particularly well suited for real-time wind field estimation in LAC applications.

Future work should investigate the effects of rotor induction and turbulence evolution on reconstruction accuracy, as these are not captured in the current setup. Additionally, evaluating the proposed methods under a broader range of atmospheric stability conditions and turbulence intensities will help further define their robustness and operational limits. To fully assess their control relevance, these reconstruction techniques should also be coupled with a flow-aware controller and tested within a feedforward individual pitch control framework, enabling quantification of potential load reductions and operational benefits. Furthermore, the proposed evaluation framework could be used to design and assess scanning strategies that maximize control authority, i.e., prioritize preview measurements that most effectively support feedforward control actions.

Appendix A: LES wind speed profile

A representation of the LES wind speed profile of the precursor is presented in Fig. A1, illustrating the two data sets used in this study, where set A represent the location from where the reference 3D turbulence fields used in HAWC2 for the hub-lidar generation were extracted, while set B shows the section from where the data to computed the global POD basis was extracted. Noticed that the lateral distance (Y) between the center of the two boxes is 751.3 m. These two datasets are referred in the overview of the methodology presented in Fig. 2.

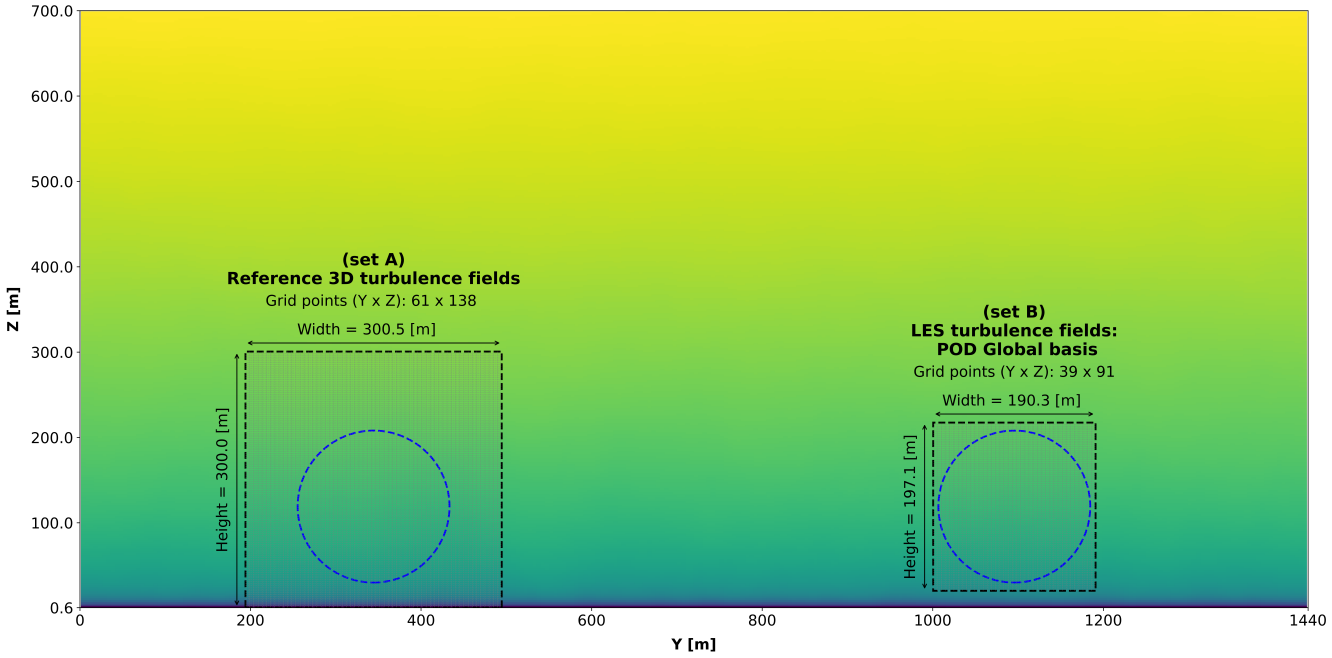

Figure A1. LES wind speed profile representation, and the two datasets used on this study, where set A represent the dataset from where the 3D turbulence fields were extracted, while set B represent the location where the dataset for the global POD modes generation was extracted.

Appendix B: Global POD modes

The global POD modes are derived from the inflow database detailed in Sect. 2.3. The first ten POD modes for the global basis are shown in Fig. B1. These modes are ranked by decreasing total kinetic energy (TKE), revealing large-scale structures in the lower-order modes that progressively diminish in size with increasing mode number. Overall, the resulting spatial modes are consistent with those previously reported for both single-wake scenarios (Sørensen et al., 2015; Bastine et al., 2018) and multiple-wake configurations (Andersen et al., 2013; Andersen and Murcia Leon, 2022).

This consistency highlights the similarity of dominant coherent structures across cases, demonstrating the potential for a reduced-order model built upon these generic patterns (Céspedes Moreno et al., 2025). However, the importance (order) of

different modes will differ across different cases, where the low-frequency fluctuations are predominant, and they disappear at higher modes (Andersen and Murcia Leon, 2022).

It is important to note that these POD modes include only the longitudinal (u) fluctuating velocity component, since this is the reconstruction target in our study.

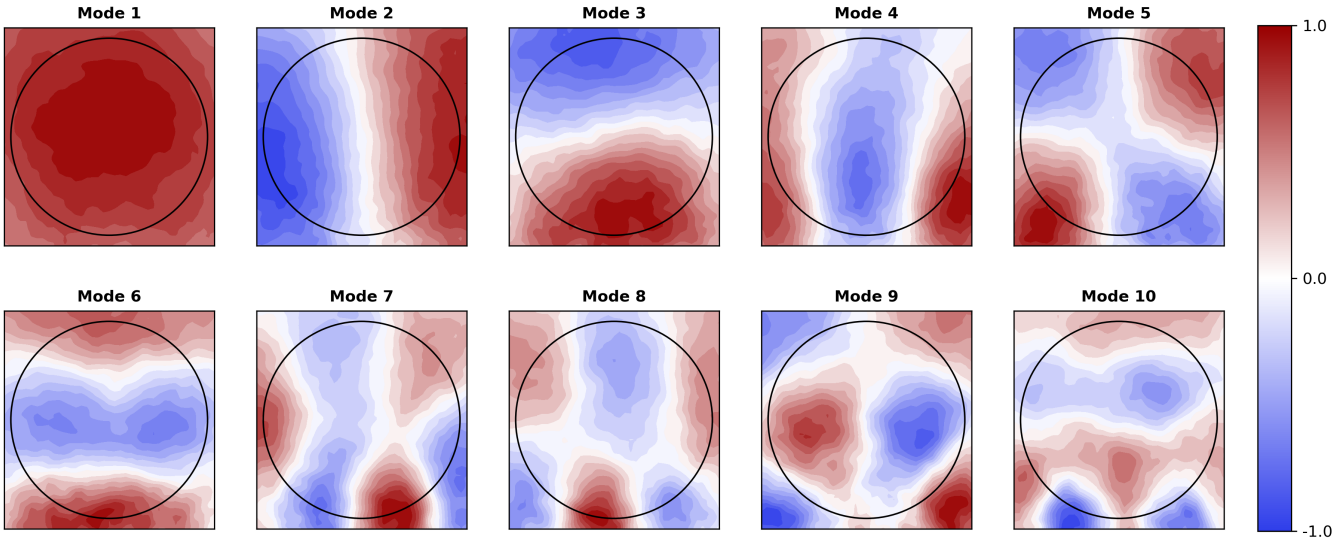

Figure B1. First 10 global POD modes, only estimated for u component.

Appendix C: Time series

To illustrate the effect of increasing the number of scans on the different reconstruction methods, Fig. C1 presents time series at a single location in the YZ plane for all evaluated methods, located at $y = -65.1\ m$ and $z = 156.1\ m$ (approximate 75% radius span). Two input cases are considered: the true wind speed (u_{fw}, solid lines) and the volume-averaged lidar estimate ($u_{\text{lidar, wgh}}$, dashed lines), both using a high scan count of $n_{\text{scan}} = 16$. This high scan count is chosen to highlight the impact of longitudinal spatial filtering, not as a practical recommendation. Above each subplot, the corresponding MAE is reported, representing the time-averaged deviation of the reconstructed signal from the LES reference signal over the full 10-minute period.

The baseline method exhibits minimal differences between the two wind speed inputs, effectively capturing the average behavior of the time series but failing to reproduce high-frequency fluctuations. This limitation reflects the method's lack of spatial and temporal adaptability. In contrast, the POD-LSQ method closely follows the LES reference in both amplitude and phase when using the true wind speed (u_{fw}). However, when using the lidar-based input ($u_{\text{lidar, wgh}}$), it captures the high-frequency variations less accurately. This is caused by the high scan number, which results in a large longitudinal span of the lidar measurements used to fit the POD amplitudes, introducing a low-pass filtering effect in the time domain. In addition, the inherent probe volume averaging of the lidar further attenuates high-frequency fluctuations (Peña et al., 2017).

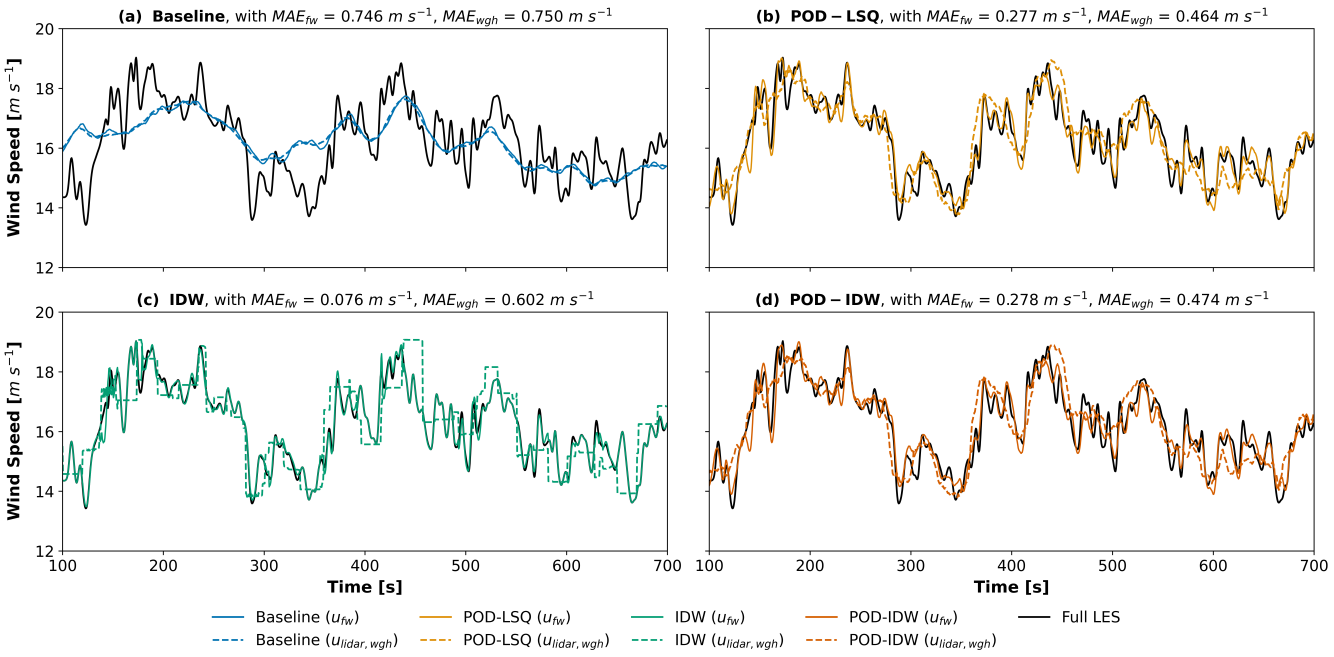

Figure C1. Comparison of 10-minute time series for each method, at a single location in $y = -65.1$ m, $z = 156.1$ m, using $n_{\text{scan}} = 16$, $\theta = 22.5°$, $K = 100$ global POD modes for POD-based methods as input parameters for the reconstruction, for the true wind speed (u_{fw}) and volume-averaged lidar estimate ($u_{\text{lidar, wgh}}$) cases.

The IDW method shows excellent agreement with the LES signal when using u_{fw}, nearly replicating the full temporal dynamics. Yet, with lidar-based input, its performance declines significantly, yielding blocky and discontinuous reconstructions that highlight its sensitivity to multi-distance fixed-plane mapping error. This is because the IDW method with u_{fw} samples the true wind at the desired YZ positions in the X_{target} plane, whereas the values of $u_{\text{lidar, wgh}}$ used for interpolation are located at different longitudinal positions. Furthermore, the values for u_{fw} used during the IDW interpolation are updated at every time step of the simulation, whereas the values for $u_{\text{lidar, wgh}}$ do not change. Thus, the time series for IDW with $u_{\text{lidar, wgh}}$ has a "quantized" look, because the point in space is being interpolated from the same measurement points, until enough time has elapsed that a new, closer measurement has acquired.

While POD-IDW performs slightly worse than POD-LSQ in terms of absolute error, it shows significantly improved robustness compared to IDW when using lidar-based inputs. By applying POD fitting on top of the interpolated IDW field, the method mitigates the blocky and discontinuous behavior introduced by direct IDW interpolation—particularly the "quantized" appearance caused by fixed measurement locations over time. This improvement stems from the projection of the IDW field onto a set of spatial patterns derived from POD, which enforces spatial coherence and smooths out interpolation artifacts. As a result, POD-IDW produces more continuous and physically consistent time series, as further illustrated in Fig. C1d.

Appendix D: Parameter sensitivity of the reconstruction methods

Figure D1 summarizes the parameter sensitivity of each reconstruction method using heat maps of the global mean absolute error, $\mathrm{MAE}_{\mathrm{global}}$. Panels (a) and (b) show Baseline and IDW as functions of the half-cone angle θ and the number of scans n_{scan}. For POD–LSQ (c) and POD–IDW (d), three parameters are involved (θ, n_{scan}, and the number of retained POD modes K); therefore, two parameters are varied at a time while the third is fixed at its method-specific optimum (see panel titles). A common color scale is used across all panels to enable direct comparisons, with darker colors indicating lower errors. For POD–LSQ, an additional color bar highlights cases exceeding the shared upper limit, $\mathrm{MAE}_{\mathrm{global}} = 0.08$.

The Baseline method is largely insensitive to θ and n_{scan}, with $\mathrm{MAE}_{\mathrm{global}}$ increasing only slightly for $\theta < 15°$. This behavior is expected because the baseline reduces the inflow to a rotor-equivalent wind speed combined with a prescribed shear profile; changes in spatial sampling or increased cross-contamination therefore have limited impact on the reconstruction. In contrast, IDW (Fig. D1b) shows a moderate dependence on both θ and n_{scan}. The lowest errors occur for intermediate half-cone angles ($17.5° < \theta < 25.0°$) and a moderate number of scans, which together improve rotor-plane coverage while maintaining an intermediate longitudinal filtering length. Overall, $\mathrm{MAE}_{\mathrm{global}}$ varies more strongly with θ than with n_{scan}, with the largest errors occurring at $\theta = 50.0°$ and $n_{\mathrm{scan}} = 1$.

POD–LSQ (Fig. D1c) is the most sensitive method, with the strongest dependence on the half-cone angle. Sensitivity increases at high mode counts because accurate reconstruction requires enough measurements per estimate, $n_{\mathrm{meas}} \geq K$, as discussed in Sect. 3.3. When this condition is not satisfied, the least-squares system becomes underdetermined and accuracy deteriorates substantially (e.g., Fig. 9c for $\theta = 50.0°$). This behavior is reflected by the orange–red regions, which denote cases beyond the shared color-scale limit ($\mathrm{MAE}_{\mathrm{global}} > 0.08$) and thus indicate pronounced performance loss. For intermediate half-cone angles ($20.0° < \theta < 27.5°$) and scan counts $n_{\mathrm{scan}} \geq 3$, POD–LSQ performs well and benefits from moderate mode truncation ($K \approx 50$).

POD–IDW (Fig. D1d) largely follows the trends observed for IDW and thus retains both its advantages and its limitations with respect to parameter selection. Low errors persist across a broad region of intermediate θ and n_{scan}, particularly for larger mode counts ($K > 50$). In this region, $\mathrm{MAE}_{\mathrm{global}}$ varies more strongly with θ than with n_{scan}. This indicates that POD–IDW is robust to reduced measurement availability and/or degraded spatial coverage, in contrast to POD–LSQ. POD–IDW achieves its lowest errors at high mode counts (here up to $K = 200$) because the POD coefficients are fitted to an IDW-reconstructed rotor-plane field rather than directly to sparse measurements, thereby avoiding the underdetermined least-squares problem that constrains POD–LSQ. However, beyond $K \approx 50$, further increases in K yield only marginal improvements in accuracy.

Overall, all three spatial reconstruction methods can markedly outperform the baseline when key parameters are selected within appropriate ranges. POD–LSQ is the most sensitive method, with accuracy strongly constrained by measurement availability and rotor-plane coverage. By contrast, IDW and POD–IDW provide consistently good performance and greater robustness; POD–IDW attains the lowest errors and is more tolerant than POD–LSQ to variations in half-cone angle and measurement selection.

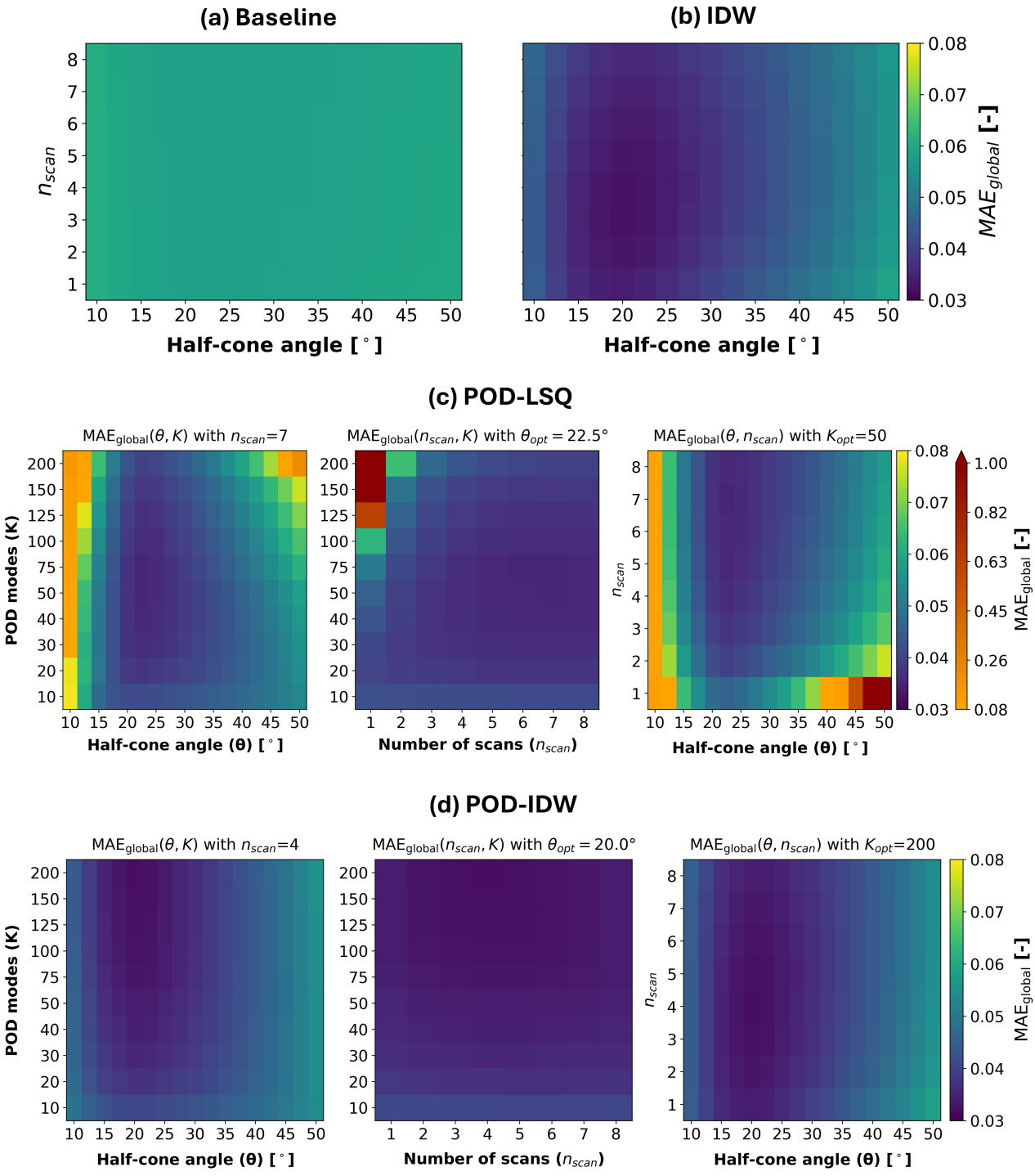

Figure D1. Heat maps of $\mathrm{MAE}_{\mathrm{global}}$, illustrating parameter sensitivity for (a) Baseline, (b) IDW, (c) POD–LSQ, and (d) POD–IDW. Baseline and IDW are shown versus θ and n_{scan}; the POD-based methods vary two of θ, n_{scan}, and K while holding the third fixed (panel titles). A common color scale is used across all panels. POD–LSQ has a second color bar indicating the cases that goes beyond the common shared color bar. Adapted from (Soto Sagredo, 2026).

Code and data availability.

The hub-lidar database generated from LES inflow simulations is available at https://doi.org/10.11583/DTU.28151724 (Soto Sagredo et al., 2025a).

Author contributions.

ES, JR, SA, and AH contributed to the conception and design of the study. ES, with input and guidance from JR, developed the HuLiDB framework, implemented and evaluated the wind field reconstruction algorithms, generated the numerical lidar database, performed the analysis, and wrote the draft manuscript. SA generated and scaled the LES inflow data and extracted the global POD modes. JR, SA, and AH provided support with the overall analysis and critically revised the manuscript.

Competing interest.

The authors declare that they have no conflict of interest.

Acknowledgments

This work is part of the CONTINUE project, which has received funding from the Danish Energy Technology Development and Demonstration Programme (EUDP) under grant agreement no. 64022-496980. The authors gratefully acknowledge the computational and data resources provided by the Technical University of Denmark through the Sophia HPC Cluster (2025) (Technical University of Denmark, 2019). We extend our sincere thanks to Michael Courtney for his critical feedback and insightful suggestions, which helped enhance the quality of this study. Finally, we acknowledge the use of OpenAI's ChatGPT (GPT-4) to support improvements in grammar, clarity, and readability during the manuscript preparation (OpenAI, 2023).

References

Andersen, S. J. and Murcia Leon, J. P.: Predictive and stochastic reduced-order modeling of wind turbine wake dynamics, Wind Energ. Sci., 7, 2117–2133, https://doi.org/10.5194/wes-7-2117-2022, 2022.

Andersen, S. J., Sørensen, J. N., and Mikkelsen, R.: Simulation of the Inherent Turbulence and Wake Interaction Inside an Infinitely Long Row of Wind Turbines, Journal of Turbulence, 14, 1–24, https://doi.org/10.1080/14685248.2013.796085, 2013.

Andersen, S. J., Sørensen, J. N., and Mikkelsen, R. F.: Turbulence and entrainment length scales in large wind farms, Philosophical Transactions of the Royal Society of London A: Mathematical, Physical and Engineering Sciences, 375, https://doi.org/10.1098/rsta.2016.0107, 2017.

Angelou, N. and Sjöholm, M.: Data Reliability Enhancement for Wind-Turbine-Mounted Lidars, Remote Sensing, 14, https://doi.org/10.3390/rs14133225, 2022.

Bak, C., Zahle, F., Bitsche, R., Kim, T., Yde, A., Henriksen, L. C., Hansen, M. H., Blasques, J. P. A. A., Gaunaa, M., and Natarajan, A.: The DTU 10-MW Reference Wind Turbine, Sound/Visual production (digital), 2013.

Bao, Y., Tan, C., and Jia, J.: Fast Dual-LiDAR Reconstruction for Dynamic Wind Field Retrieval, Atmosphere, 13, https://doi.org/10.3390/atmos13060905, 2022.

Bastine, D., Vollmer, L., Wächter, M., and Peinke, J.: Stochastic Wake Modelling Based on POD Analysis, Energies, 11, 1–29, https://doi.org/10.3390/en11030612, 2018.

Bauweraerts, P. and Meyers, J.: Bayesian based estimation of turbulent flow fields from lidar observations in a conventionally neutral atmospheric boundary layer, Journal of Physics: Conference Series, 1618, 032 047, https://doi.org/10.1088/1742-6596/1618/3/032047, 2020.

Bauweraerts, P. and Meyers, J.: Reconstruction of turbulent flow fields from lidar measurements using large-eddy simulation, Journal of Fluid Mechanics, 906, A17, https://doi.org/10.1017/jfm.2020.805, 2021.

Beck, H. and Kühn, M.: Temporal Up-Sampling of Planar Long-Range Doppler LiDAR Wind Speed Measurements Using Space-Time Conversion, Remote Sensing, 11, 867, https://doi.org/10.3390/rs11070867, 2019.

Berkooz, G., Holmes, P., and Lumley, J. L.: The proper orthogonal decomposition in the analysis of turbulent flows, Annual Review of Fluid Mechanics, 25, 539–575, https://doi.org/10.1146/annurev.fl.25.010193.002543, 1993.

Bokati, L., Velasco, A., and Kreinovich, V.: Scale-Invariance and Fuzzy Techniques Explain the Empirical Success of Inverse Distance Weighting and of Dual Inverse Distance Weighting in Geosciences, in: Bede, B., Ceberio, M., De Cock, M., Kreinovich, V. (eds) Fuzzy Information Processing 2020. NAFIPS 2020. Advances in Intelligent Systems and Computing, vol. 1337, pp. 379–390, Springer International Publishing, Cham, https://doi.org/10.1007/978-3-030-81561-5_32, 2022.

Borraccino, A., Schlipf, D., Haizmann, F., and Wagner, R.: Wind field reconstruction from nacelle-mounted lidar short-range measurements, Wind Energ. Sci., 2, 269–283, https://doi.org/10.5194/wes-2-269-2017, 2017.

Bossanyi, E.: Un-freezing the turbulence: application to LiDAR-assisted wind turbine control, IET Renewable Power Generation, 7, 321–329, https://doi.org/https://doi.org/10.1049/iet-rpg.2012.0260, 2013.

Bossanyi, E. A., Kumar, A., and Hugues-Salas, O.: Wind turbine control applications of turbine-mounted LIDAR, Journal of Physics: Conference Series, 555, 012 011, https://doi.org/10.1088/1742-6596/555/1/012011, 2012.

Canet, H., Loew, S., and Bottasso, C. L.: What are the benefits of lidar-assisted control in the design of a wind turbine?, Wind Energ. Sci., 6, 1325–1340, https://doi.org/10.5194/wes-6-1325-2021, 2021.

Castro, I.: Rough-wall boundary layers: Mean flow universality, J. Fluid Mech, 585, 469–485, https://doi.org/10.1017/S0022112007006921, 2007.

Céspedes Moreno, J. F., Murcia León, J. P., and Andersen, S. J.: Convergence and efficiency of global bases using proper orthogonal decomposition for capturing wind turbine wake aerodynamics, Wind Energ. Sci., 10, 597–611, https://doi.org/10.5194/wes-10-597-2025, 2025.

Chu, J., Han, Y., Sun, D., Han, F., and Liu, H.: Statistical interpolation technique based on coherent Doppler lidar for real-time horizontal wind shear observations and forewarning, Optical Engineering, 60, 046 102, https://doi.org/10.1117/1.OE.60.4.046102, 2021.

De Cillis, G., Cherubini, S., Semeraro, O., Leonardi, S., and De Palma, P.: POD analysis of the recovery process in wind turbine wakes, Journal of Physics: Conference Series, 1618, 062 016, https://doi.org/10.1088/1742-6596/1618/6/062016, 2020.

de Maré, M. and Mann, J.: On the Space-Time Structure of Sheared Turbulence, Boundary-Layer Meteorology, 160, 453–474, https://doi.org/10.1007/s10546-016-0143-z, 2016.

Dimitrov, N. and Natarajan, A.: Application of simulated lidar scanning patterns to constrained Gaussian turbulence fields for load validation, Wind Energy, 20, 79–95, https://doi.org/10.1002/we.1992, 2016.

Dimitrov, N., Kelly, M. C., Vignaroli, A., and Berg, J.: From wind to loads: Wind turbine site-specific load estimation with surrogate models trained on high-fidelity load databases, Wind Energ. Sci., 3, 767–790, https://doi.org/10.5194/wes-3-767-2018, 2018.

Dong, L., Lio, W. H., and Simley, E.: On turbulence models and lidar measurements for wind turbine control, Wind Energ. Sci., 6, 1491–1500, https://doi.org/10.5194/wes-6-1491-2021, 2021.

Doubrawa, P., Churchfield, M. J., Godvik, M., and Sirnivas, S.: Load response of a floating wind turbine to turbulent atmospheric flow, Applied Energy, 242, 1588–1599, https://doi.org/10.1016/j.apenergy.2019.01.165, 2019.

DTU Wind Energy: HAWC2 Horizontal Axis Wind turbine simulation Code 2nd generation, https://tools.windenergy.dtu.dk/home/HAWC2/, accessed: 2025-04-11, 2024.

Dunne, F., Pao, L. Y., Wright, A., Jonkman, B., Kelley, N., and Simley, E.: Adding feedforward blade pitch control for load mitigation in wind turbines: non-causal series expansion, preview control, and optimized fir filter methods, 49th AIAA Aerospace Sciences Meeting Including the New Horizons Forum and Aerospace Exposition, https://doi.org/10.2514/6.2011-819, 2011.

Dunne, F., Schlipf, D., Pao, L., et al.: Comparison of two independent LIDAR-based pitch control designs, in: 50th AIAA Aerospace Sciences Meeting Including the New Horizons Forum and Aerospace Exposition, p. 2012:1151, American Institute of Aeronautics and Astronautics, https://doi.org/10.2514/6.2012-1151, 2012.

Friedland, C. J., Joyner, T. A., Massarra, C., Rohli, R. V., Treviño, A. M., Ghosh, S., Huyck, C., and Weatherhead, M.: Isotropic and anisotropic kriging approaches for interpolating surface-level wind speeds across large, geographically diverse regions, Geomatics Natural Hazards and Risk, 8, 207–224, https://doi.org/10.1080/19475705.2016.1185749, 2016.

Fu, W., Guo, F., Schlipf, D., and Peña, A.: Feedforward pitch control for a 15 MW wind turbine using a spinner-mounted single-beam lidar, Wind Energ. Sci., 8, 1893–1907, https://doi.org/10.5194/wes-8-1893-2023, 2023.

Fu, W. et al.: Influence of nacelle-lidar scanning patterns on inflow turbulence characterization, in: Journal of Physics: Conference Series, vol. 2265, p. 022016, IOP Publishing, https://doi.org/10.1088/1742-6596/2265/2/022016, 2022.

Gräfe, M., Pettas, V., Gottschall, J., and Cheng, P. W.: Quantification and correction of motion influence for nacelle-based lidar systems on floating wind turbines, Wind Energ. Sci., 8, 925–946, https://doi.org/10.5194/wes-8-925-2023, 2023.

Guo, F., Mann, J., Peña, A., Schlipf, D., and Cheng, P. W.: The space-time structure of turbulence for lidar-assisted wind turbine control, Renewable Energy, 195, 293–310, https://doi.org/10.1016/j.renene.2022.05.133, 2022.

Guo, F., Schlipf, D., and Cheng, P. W.: Evaluation of lidar-assisted wind turbine control under various turbulence characteristics, Wind Energ. Sci., 8, 149–171, https://doi.org/10.5194/wes-8-149-2023, 2023.

Halko, N., Martinsson, P. G., and Tropp, J. A.: Finding Structure with Randomness: Probabilistic Algorithms for Constructing Approximate Matrix Decompositions, SIAM Review, 53, 217–288, https://doi.org/10.1137/090771806, 2011.

Hamilton, N., Doubrawa, P., Moriarty, P., Letizia, S., and Thedin, R.: Modal dynamics of wind turbine wake meandering from lidar observations, Renewable Energy, 254, 123 555, https://doi.org/https://doi.org/10.1016/j.renene.2025.123555, 2025.

Held, D. P. and Mann, J.: Lidar estimation of rotor-effective wind speed – an experimental comparison, Wind Energ. Sci., 4, 421–438, https://doi.org/10.5194/wes-4-421-2019, 2019.

Herges, T. G., Maniaci, D. C., Naughton, B. T., Mikkelsen, T., and Sjöholm, M.: High resolution wind turbine wake measurements with a scanning lidar, in: Journal of Physics: Conference Series, vol. 854, p. 012021, IOP Publishing, https://doi.org/10.1088/1742-6596/854/1/012021, 2017.

Iqbal, M. O. and Thomas, F. O.: Coherent structure in a turbulent jet via a vector implementation of the proper orthogonal decomposition, Journal of Fluid Mechanics, 571, 281–326, https://doi.org/10.1017/S0022112006003351, 2007.

Joyner, T. A., Friedland, C. J., Rohli, R. V., Treviño, A. M., Massarra, C., and Paulus, G.: Cross-correlation modeling of european windstorms: a cokriging approach for optimizing surface wind estimates, Spatial Statistics, 13, 62–75, https://doi.org/10.1016/j.spasta.2015.05.003, 2015.

Kelberlau, F. and Mann, J.: Cross-contamination effect on turbulence spectra from Doppler beam swinging wind lidar, Wind Energ. Sci., 5, 519–541, https://doi.org/10.5194/wes-5-519-2020, 2020.

Kidambi Sekar, A. P., van Dooren, M. F., Rott, A., and Kühn, M.: Lower Order Description and Reconstruction of Sparse Scanning Lidar Measurements of Wind Turbine Inflow Using Proper Orthogonal Decomposition, Remote Sensing, 14, 2681, https://doi.org/10.3390/rs14112681, 2022.

Letizia, S., Brugger, P., Bodini, N., Krishnamurthy, R., Scholbrock, A., Simley, E., Porté-Agel, F., Hamilton, N., Doubrawa, P., and Moriarty, P.: Characterization of wind turbine flow through nacelle-mounted lidars: a review, https://doi.org/10.3389/fmech.2023.1261017, 2023.

Li, Z., Zhang, X., Zhu, R., Zhang, Z., and Weng, Z.: Integrating data-to-data correlation into inverse distance weighting, Computational Geosciences, 24, 203–216, https://doi.org/10.1007/s10596-019-09913-9, 2020.

Liverud Krathe, V., Jonkman, J., Gebel, J., Rivera-Arreba, I., Nejad, A., and Bachynski-Polić, E.: Investigation of Main Bearing Fatigue Estimate Sensitivity to Synthetic Turbulence Models Using a Novel Drivetrain Model Implemented in OpenFAST, Wind Energy, 28, e70 005, https://doi.org/10.1002/we.70005, 2025.

Lumley, J. L.: The Structure of Inhomogeneous Turbulence, in: Atmospheric Turbulence and Wave Propagation, pp. 166–178, Nauka, Moscow, ISBN 9783937655239, 1967.

Luo, W., Taylor, M., and Parker, S.: A comparison of spatial interpolation methods to estimate continuous wind speed surfaces using irregularly distributed data from england and wales, International Journal of Climatology, 28, 947–959, https://doi.org/10.1002/joc.1583, 2007.

Mann, J.: Wind field simulation, Probabilistic Engineering Mechanics, 13, 269–282, https://doi.org/10.1016/S0266-8920(97)00036-2, 1998.

Mann, J., Penã, A., Troldborg, N., and Andersen, S. J.: How does turbulence change approaching a rotor?, Wind Energ. Sci., 3, 293–300, https://doi.org/10.5194/wes-3-293-2018, 2018.

Meneveau, C.: Big wind power: seven questions for turbulence research, Journal of Turbulence, 20, 2–20, https://doi.org/10.1080/14685248.2019.1584664, 2019.

Meyer Forsting, A. R., Troldborg, N., and Borraccino, A.: Modelling lidar volume-averaging and its significance to wind turbine wake measurements, in: Journal of Physics: Conference Series, vol. 854, p. 012014, Institute of Physics Publishing, https://doi.org/10.1088/1742-6596/854/1/012014, 2017.

Michelsen, J. A.: Basis3D - a Platform for Development of Multiblock PDE Solvers: β - release, Technical report, Technical University of Denmark, 1992.

Michelsen, J. A.: Block structured Multigrid solution of 2D and 3D elliptic PDE's, Technical Report AFM 94-06, Technical University of Denmark, 1994.

Mikkelsen, T., Angelou, N., Hansen, K., Sjöholm, M., Harris, M., Slinger, C., Hadley, P., Scullion, R., Ellis, G., and Vives, G.: A spinner integrated wind lidar for enhanced wind turbine control, Wind Energy, 16, 625–643, https://doi.org/10.1002/we.1564, 2013.

Moore, E. H.: On the reciprocal of the general algebraic matrix, Bulletin of the American Mathematical Society, 26, 394–395, 1920.

Munters, W., Meneveau, C., and Meyers, J.: Shifted periodic boundary conditions for simulations of wall-bounded turbulent flows, Physics of Fluids, 28, 025 112, https://doi.org/10.1063/1.4941912, 2016.

Newman, A. J., Drew, D. A., and Castillo, L.: Pseudo spectral analysis of the energy entrainment in a scaled down wind farm, Renewable Energy, 70, 129–141, https://doi.org/https://doi.org/10.1016/j.renene.2014.02.003, 2014.

OpenAI: GPT-4 Technical Report, https://doi.org/10.48550/arXiv.2303.08774, https://doi.org/10.48550/arXiv.2303.08774, accessed July 2025, 2023.

Peña, A., Mann, J., and Dimitrov, N.: Turbulence characterization from a forward-looking nacelle lidar, Wind Energ. Sci., 2, 133–152, https://doi.org/10.5194/wes-2-133-2017, 2017.

Peña, A., Hasager, C. B., Lange, J., Anger, J., Badger, M., Bingöl, F., Bischoff, O., Cariou, J.-P., Dunne, F., Emeis, S., Harris, M., Hofsäss, M., Karagali, I., Laks, J., Larsen, S. E., Mann, J., Mikkelsen, T., Pao, L. Y., Pitter, M., and Würth, I.: Remote Sensing for Wind Energy, Tech. Rep. E No. 0029(EN), DTU Wind Energy, 2013.

Peña, A., Hasager, C., Badger, M., Barthelmie, R., Bingöl, F., Cariou, J.-P., Emeis, S., Frandsen, S., Harris, M., Karagali, I., Larsen, S., Mann, J., Mikkelsen, T., Pitter, M., Pryor, S., Sathe, A., Schlipf, D., Slinger, C., and Wagner, R.: Remote sensing for wind energy, Tech. rep., DTU Wind Energy, 2015.

Penrose, R.: A generalized inverse for matrices, Proceedings of the Cambridge Philosophical Society, 51, 406–413, 1955.

Raach, S., Schlipf, D., Haizmann, F., and Cheng, P. W.: Three Dimensional Dynamic Model Based Wind Field Reconstruction from Lidar Data, Journal of Physics: Conference Series, 524, 012 005, https://doi.org/10.1088/1742-6596/524/1/012005, 2014.

Rinker, J. M.: Impact of rotor size on aeroelastic uncertainty with lidar-constrained turbulence, in: Journal of Physics: Conference Series, vol. 2265, p. 032011, IOP Publishing, https://doi.org/10.1088/1742-6596/2265/3/032011, 2022.

Rivera-Arreba, I., Wise, A. S., Hermile, M., Chow, F. K., and Bachynski-Polić, E. E.: Effects of atmospheric stability on the structural response of a 12 MW semisubmersible floating wind turbine, Wind Energy, 25, 1917–1937, https://doi.org/10.1002/we.2775, 2022.

Russell, A. J., Collu, M., McDonald, A. S., Thies, P. R., Keane, A., and Quayle, A. R.: Lidar-assisted feedforward individual pitch control of a 15 mw floating offshore wind turbine, Wind Energy, 27, 341–362, https://doi.org/10.1002/we.2891, 2024.

Sathe, A., Banta, R., Pauscher, L., Vogstad, K., Schlipf, D., and Wylie, S.: Estimating turbulence statistics and parameters from ground- and nacelle-based lidar measurements: IEA wind expert report, Tech. Rep. Grant no: 0602-02486B, DTU Wind Energy, 2015.

Schlipf, D.: Lidar-Assisted Control Concepts for Wind Turbines, Ph.d. thesis, University of Stuttgart, Institute of Aircraft Design, University of Stuttgart, https://doi.org/10.18419/opus-8796, 2016.

Schlipf, D. and Kühn, M.: Prospects of a collective pitch control by means of predictive disturbance compensation assisted by wind speed measurements, in: Proceedings of the 9th German Wind Energy Conference DEWEK 2008, 26th to 27th November, Bremen, Germany, http://dx.doi.org/10.18419/opus-3900, 2008.

Schlipf, D., Schuler, S., Grau, P., Allgöwer, F., and Kühn, M.: Look-ahead cyclic pitch control using lidar, in: Proceedings of the Science of Making Torque from Wind 2010, Crete, Greece, http://dx.doi.org/10.18419/opus-4538, 2010.

Schlipf, D., Schlipf, D. J., and Kühn, M.: Nonlinear model predictive control of wind turbines using LIDAR, Wind Energy, 16, 1107–1129, https://doi.org/10.1002/we.1533, 2013.

Schlipf, D., Haizmann, F., Cosack, N., Siebers, T., and Cheng, P. W.: Detection of Wind Evolution and Lidar Trajectory Optimization for Lidar-Assisted Wind Turbine Control, Meteorologische Zeitschrift, 24, 565–579, https://doi.org/10.1127/metz/2015/0634, 2015.

Schlipf, D., Hille, N., Raach, S., Scholbrock, A., and Simley, E.: IEA Wind Task 32: Best Practices for the Certification of Lidar-Assisted Control Applications, in: Journal of Physics: Conference Series, vol. 1102, p. 012010, IOP Publishing, ISSN 17426596, https://doi.org/10.1088/1742-6596/1102/1/012010, 2018.

Scholbrock, A., Fleming, P., Schlipf, D., Wright, A., Johnson, K., and Wang, N.: Lidar-enhanced wind turbine control: past, present, and future, 2016 American Control Conference (ACC), 555, 1399–1406, https://doi.org/10.1109/acc.2016.7525113, 2016.

Sebastiani, A., Peña, A., and Troldborg, N.: Wind turbine power performance characterization through aeroelastic simulations and virtual nacelle lidar measurements, Journal of Physics: Conference Series, 2265, 022 059, https://doi.org/10.1088/1742-6596/2265/2/022059, 2022.

Sekar, A. P. K., van Dooren, M. F., and Kühn, M.: Overcoming blade interference: a gappy-pod data reconstruction method for nacelle-mounted lidar measurements, Journal of Physics: Conference Series, 2265, 022 078, https://doi.org/10.1088/1742-6596/2265/2/022078, 2022.

Simley, E., Pao, L., Frehlich, R., Jonkman, B., and Kelley, N.: Analysis of Wind Speed Measurements using Continuous Wave LIDAR for Wind Turbine Control, in: 49th AIAA Aerospace Sciences Meeting including the New Horizons Forum and Aerospace Exposition, Orlando, Florida, https://doi.org/10.2514/6.2011-263, 2011.

Simley, E., Pao, L. Y., Kelley, N., Jonkman, B., and Frehlich, R.: LIDAR wind speed measurements of evolving wind fields, in: 50th AIAA Aerospace Sciences Meeting Including the New Horizons Forum and Aerospace Exposition, AIAA, Nashville, Tennessee, https://doi.org/10.2514/6.2012-656, 2012.

Simley, E., Pao, L. Y., Frehlich, R., Jonkman, B., and Kelley, N.: Analysis of light detection and ranging wind speed measurements for wind turbine control, Wind Energy, 17, 413–433, https://doi.org/10.1002/we.1584, 2014.

Simley, E., Fürst, H., Haizmann, F., and Schlipf, D.: Optimizing Lidars for Wind Turbine Control Applications—Results from the IEA Wind Task 32 Workshop, Remote Sensing, 10, 863, https://doi.org/10.3390/rs10060863, 2018.

Soto Sagredo, E., Rinker, J. M., and Lund, R. S.: Verification of numerical lidars in HAWC2: Analysis of nacelle- and hub-mounted lidars, Tech. Rep. E-0239, DTU Wind Energy, https://doi.org/10.11581/DTU.00000302, 2023.

Soto Sagredo, E., Rinker, J. M., Andersen, S. J., and Forrest, J. P.: Wind-field characterization using synthetic lidar measurements and proper orthogonal decomposition, Journal of Physics: Conference Series, 2767, 052 061, https://doi.org/10.1088/1742-6596/2767/5/052061, 2024a.

Soto Sagredo, E., Rinker, J. M., and Andersen, S. J.: Numerical hub-lidar data from LES-generated turbulence boxes using HAWC2 v13.1 and DTU 10MW reference wind turbine, https://doi.org/10.11583/DTU.28151724, dataset, 2025a.

Soto Sagredo, E., Rinker, J. M., Hannesdóttir, A., and Courtney, M.: Numerical evaluation of the smearing effect in a spinner-mounted lidar for wind field reconstruction, Journal of Physics: Conference Series, 3025, 012 006, https://doi.org/10.1088/1742-6596/3025/1/012006, 2025b.

Soto Sagredo, E. A.: Wind field reconstruction methods for a hub-mounted lidar, Phd thesis, DTU Wind and Energy Systems, Technical University of Denmark, https://doi.org/10.11581/6ada55bf-2225-4f18-89d2-bf50696949f7, accepted/In press, 2026.

Soto Sagredo, E. A., Hannesdóttir, A., Rinker, J. M., and Courtney, M.: Reconstructing turbulent wind-fields using inverse-distance-weighting interpolation and measurements from a pulsed mounted-hub lidar, Journal of Physics: Conference Series, 2745, 012 017, https://doi.org/10.1088/1742-6596/2745/1/012017, 2024b.

Sørensen, J. N., Mikkelsen, R. F., Henningson, D. S., Ivanell, S., Sarmast, S., and Andersen, S. J.: Simulation of Wind Turbine Wakes Using the Actuator Line Technique, Philosophical Transactions of the Royal Society A: Mathematical, Physical and Engineering Sciences, 373, 20140 071, https://doi.org/10.1098/rsta.2014.0071, 2015.

Sørensen, N. N.: General purpose flow solver applied to flow over hills, Risø National Laboratory, ISBN 8755020798, 9788755020795, 1995.

Taylor, G. I.: The Spectrum of Turbulence, Proceedings of the Royal Society of London. Series A - Mathematical and Physical Sciences, 164, 476–490, https://doi.org/10.1098/rspa.1938.0032, 1938.

Technical University of Denmark: Sophia HPC Cluster, https://doi.org/10.57940/FAFC-6M81, 2019.

Thedin, R., Quon, E., Churchfield, M., and Veers, P.: Investigations of correlation and coherence in turbulence from a large-eddy simulation, Wind Energ. Sci., 8, 487–502, https://doi.org/10.5194/wes-8-487-2023, 2023.

Troldborg, N., Andersen, S. J., Hodgson, E. L., and Meyer Forsting, A.: Brief communication: How does complex terrain change the power curve of a wind turbine?, Wind Energ. Sci., 7, 1527–1532, https://doi.org/10.5194/wes-7-1527-2022, 2022.

VerHulst, C. and Meneveau, C.: Large eddy simulation study of the kinetic energy entrainment by energetic turbulent flow structures in large wind farms, Physics of Fluids, 26, 025 113, https://doi.org/10.1063/1.4865755, 2014.

Zhang, J. and Zhao, X.: Spatiotemporal wind field prediction based on physics-informed deep learning and LIDAR measurements, Applied Energy, 288, 116 641, https://doi.org/10.1016/j.apenergy.2021.116641, 2021a.

Zhang, J. and Zhao, X.: Three-dimensional spatiotemporal wind field reconstruction based on physics-informed deep learning, Applied Energy, 300, 117 390, https://doi.org/10.1016/j.apenergy.2021.117390, 2021b.